J. Fluid Mech. (2006), *vol.* 546, *pp.* 153–191. © 2005 Cambridge University Press
doi:10.1017/S0022112005006993 Printed in the United Kingdom

Direct numerical simulations of variable-density plane jets

By STÉPHANE RAVIER, MALEK ABID, MURIEL AMIELH AND FABIEN ANSELMET

Institut de Recherche sur les Phénomènes Hors-Équilibre, CNRS–UMR 6594,
49 rue Frédéric Joliot-Curie, BP 146, F-13384 Marseille Cedex 13, France

(Received 22 April 2004 and in revised form 30 June 2005)

Two-dimensional incompressible and heterogeneous free jets are studied numerically. They are characterized by two linearly unstable modes: the sinuous mode and the varicose mode. When the density is constant, the sinuous mode dominates, in a sense that it has a maximum growth rate nearly three times greater than that of the varicose mode, both in the temporal and spatial stability frameworks. This suggests that jet evolution at the linear and nonlinear regimes, at least at early stage, would be sinuous with the frequency and wavenumber of the most unstable mode. This is confirmed in the present work. When the jet density is decreased, it is found that the varicose mode growth rate is enhanced and its maximum value can exceed that of the sinuous mode. Furthermore, in the spatial case, only the varicose mode is subject to a convective/absolute instability transition. It is shown, however, that the maximum varicose growth rate exceeds that of the sinuous mode before the transition occurs. Therefore, a natural question is: does the convective/absolute transition dictate its frequency to the nonlinear evolution of the jet, leading to a global oscillating varicose mode, or is it, simply, the frequency of the maximum varicose growth rate that does? The main part of this paper is devoted to answering this question by direct numerical simulation for a wide range of jet-exit to ambient density ratios.

1. Introduction

Jet flows, and more precisely their near-field large-scale structures, are widely studied in the literature either from a numerical or an experimental point of view. They are of great interest as prototypes of laminar/turbulent transition, particularly in aerospace and combustion applications aimed at enhancing mixing. Evidently, two-dimensional jets are a first step towards the understanding of the more realistic, but complex, three-dimensional jets and, surprisingly, to the best of our knowledge, no one has published results on direct numerical simulation of incompressible variable-density two-dimensional jets. Those facts motivated the choice of the dimensionality of the problem in the present study.

The most attractive phenomenon observed in jet flows is that lowering the jet density, relative to the ambient, leads to self-excited oscillations or global instability of the jet. Such oscillations, characterized by line-dominated power spectra as opposed to the broad-band ones in the constant density case, were discovered experimentally by Sreenivasan, Raghu & Kyle (1989) and Kyle & Sreenivasan (1993), in a round helium–air jet, and by Monkewitz *et al.* (1990) in a heated air jet. Yu & Monkewitz (1993) showed the same behaviour for the low-density two-dimensional hot jets. The intrinsic character of these low-density jet oscillations and its insensitivity to small perturbations were also revealed.

For the two-dimensional hot jet, Yu & Monkewitz found a critical jet to ambient density ratio, s_{ca}, approximately equal to 0.9 below which the jet is self-excited. They tried to link it to the threshold of convective/absolute transition obtained in their previous work on linear stability of jets and wakes (Yu & Monkewitz 1990).

The concept of convective and absolute instability goes back to the works of Twiss (1951) and Landau & Lifshitz (1959) who first pointed out that a pulsed disturbance in an unstable medium can evolve in two distinct physical ways.

(i) The pulse can grow and propagate away from its origin so that at a fixed point in space the disturbance eventually decays with time: this is *convective instability.*

(ii) The pulse can contaminate more and more of the space leading to a disturbance growth with time at eventually every point in space: this is a non-convective, also called *absolute instability.*

In the linear regime, it is sufficient to determine the Green function (space–time impulse response), $G(\boldsymbol{r}, t)$, of the linearized equations describing a particular medium to obtain insight on instability that grows from small-amplitude disturbances. For one-dimensional infinitely extended medium, say along x, the Fourier–Laplace transform of the Green function is given by:

$$G(k, \omega; s) = \frac{1}{D(k, \omega; s)}, \tag{1.1}$$

where k stands for a complex wavenumber, $\omega/(2\pi)$ a complex frequency, s a control parameter (the jet-exit to ambient density ratio in the present work) and $D(k, \omega; s)$ for the Fourier–Laplace transform of the linear operator. It is clear from equation (1.1) that the singularities (also called dispersion relations) $\omega = \omega(k; s)$ or $k = k(\omega; s)$, solutions of $D(k, \omega; s) = 0$, play an important role in the expression of $G(x, t; s)$. Particularly, poles of order 2 in k, (also double roots in k of D) solutions of

$$D(k_0, \omega_0; s) = 0, \quad \frac{\partial D(k_0, \omega_0; s)}{\partial k} = 0, \tag{1.2}$$

when they correspond to the merging, or the 'pinching', of two roots: $k_\ell(\omega; s)$ and $k_u(\omega; s)$, originating from the lower- and upper-half complex k-plane, respectively (and only in that case), are of great importance. Indeed it is shown, elegantly, in Bers (1983) that the time-asymptotic Green function is dominated by the integration around the pinch-point singularity $\omega_0(s)$ that has the maximum imaginary part. This integration leads to:

$$\lim_{t\to\infty} G(x, t; s) \sim \exp(\mathrm{i}k_0(s)x)\frac{\exp(-\mathrm{i}\omega_0(s)t)}{t^{1/2}} \quad \text{for all} \quad x, \tag{1.3}$$

which is a single (global) Fourier mode tuned at a well-defined frequency. Note that a Taylor expansion of D centred at (ω_0, k_0) along one singularity curve gives

$$a(\omega - \omega_0) + b(k - k_0)^2 + O((\omega - \omega_0)^2, (k - k_0)^3) = 0, \quad (a, b) \in \mathbb{C}^2,$$

showing that $v_g(k_0) = (\partial\omega/\partial k)\ (k_0) = 0$ where $v_g(k_0)$ is the group velocity of the wave packet centred at k_0. (No perturbations of zero group velocity, in a fixed laboratory reference frame, have ever been observed experimentally for open shear flows however (E. Villermaux, personal communication, 2003).)

The critical value s_{ca} of s for which $\mathrm{Im}\,(\omega_0(s_{ca})) = 0$ is the signature of convective/absolute transition according to the previously given definitions. Yu & Monkewitz, in their above-mentioned linear study, computed a density ratio $s_{ca} = 0.95$ below which two-dimensional variable-density jets become absolutely unstable. It is in good agreement with $s_{ca} = 0.9$ obtained experimentally. There was agreement until the work of Raynal *et al.* (1996). They found $s_{ca} = 0.7$ for a helium–air jet, which disagrees with linear theory and the experiments of Yu & Monkewitz. They considered differences in shape and relative positions of the density and velocity profiles to explain the discrepancy. However, as density profiles are not easily accessible experimentally, their arguments remain hypothetical ones.

The pertinence of convective/absolute concepts to the nonlinear evolution, especially for media governed by the full incompressible Navier–Stokes equations, has been addressed by Delbende & Chomaz (1998) at first. They considered the fully nonlinear impulse response by direct numerical simulations. They showed, for a family of plane wake profiles at low Reynolds numbers, that nonlinear terms limit the amplitude to a saturation level within the linear response wave packet leaving the trailing and leading edges unaffected. They concluded that the velocities of the fronts are thus selected according to the linear Dee and Langer ‘marginal stability’ conjecture (Dee & Langer 1983) although the front solutions are fully nonlinear. Note that Delbende & Chomaz used a fixed homogeneous parallel basic flow in all their simulations. Therefore, the retroaction of the growing perturbation on the basic profile is not considered and this is, to some extent, a forcing. Later, Pier & Huerre (2001) considered a ‘synthetic’ family of weakly spatially developing, constant density wakes with no recirculating flow region. They showed, numerically, that these profiles sustain a synchronized finite-amplitude vortex street tuned at a well-defined frequency. Although the vortex street is fully nonlinear, its frequency is dictated by a purely linear marginal absolute instability criterion from the local linear dispersion relation. Note that the basic flows used by Pier & Huerre are also fixed in all their simulations.

In the present work, the constraints fixed in the works of Delbende, Chomaz, Pier and Huerre are relaxed: free spatially evolving variable-density jets are numerically considered.

The paper is organized as follows: general formulation is presented in § 2. The linear instability analysis together with convective/absolute transition, for a wide range of density ratios and different velocity profiles, are addressed in § 3. The nonlinear study follows in § 4 where the numerical method is presented with particular attention devoted to the boundary conditions and to the validation of the method. In the same section, main results on the relevance of the linearly determined critical density ratios and the corresponding frequencies are also presented. Finally, conclusions are drawn in § 5.

2. General formulation

This study deals with a variable-density plane jet. This kind of jet can be achieved by pushing helium, with some experimental facility, into the ambient air, for example. The flow is supposed to be incompressible. In addition buoyancy, gravity, thermal and surface-tension effects are neglected. Following experimental results for gaseous fluids, the dynamic viscosity μ is constant. If $\boldsymbol{v}$ represents the velocity field, p the pressure and ρ the density, the governing equations are

$$\left.\begin{aligned}
&\frac{\partial \boldsymbol{v}}{\partial t} + (\boldsymbol{v}\cdot\nabla)\boldsymbol{v} = -\frac{1}{\rho}\nabla p + \frac{\mu}{\rho}\Delta \boldsymbol{v},\\
&\nabla\cdot\boldsymbol{v} = 0,\\
&\frac{\partial \rho}{\partial t} + (\boldsymbol{v}\cdot\nabla)\rho = 0.
\end{aligned}\right\} \qquad (2.1)$$

Let $\bar{L}$, $\bar{U}$, $\bar{\rho}$ and $\bar{\mu}$ be length, velocity, density and viscosity scales, respectively. With these scales, we can define dimensionless quantities such as $t^* = \bar{U}t/\bar{L}$ and a specific Reynolds number $Re = \bar{\rho}\bar{U}\bar{L}/\bar{\mu}$ which is called the 'calculus' Reynolds number. If the scales are precisely defined, we can compare this number with a flow Reynolds number in experiments. For this work, $\bar{L}$ is the jet half-velocity generalized radius, $\bar{U}$ is the maximum jet velocity and $\bar{\rho}$ is the ambient density. The Reynolds number based on the ambient air dynamic viscosity is then exactly that used by Yu & Monkewitz (1990, 1993), but is different from the definition used by Raynal *et al.* (1996).

From now on, all the quantities are dimensionless, but the same notations as for the dimensional ones are used (the asterisks are omitted). So, (2.1) becomes

$$\left.\begin{aligned} &\frac{\partial \boldsymbol{v}}{\partial t} + (\boldsymbol{v}\cdot\nabla)\boldsymbol{v} = -\frac{1}{\rho}\nabla p + \frac{1}{\rho}\frac{1}{Re}\Delta\boldsymbol{v},\\ &\nabla\cdot\boldsymbol{v} = 0,\\ &\frac{\partial \rho}{\partial t} + (\boldsymbol{v}\cdot\nabla)\rho = 0. \end{aligned}\right\} \tag{2.2}$$

Unless otherwise mentioned, $Re = 1000$ is used.

3. Linear analysis

In this section, the work done by Yu & Monkewitz (1990) on linear instability of variable-density, parallel plane jets is extended. The convective/absolute density ratio transition of the Bickley jet, which is not given in Yu & Monkewitz, is computed. The question of the coexistence of varicose and sinuous modes, which has not been studied so far, is also addressed by comparison of maximum growth rates of the two modes for different values of the density ratio. Furthermore, temporal dispersion relations that will be used to test the nonlinear study are given.

3.1. *Outline of the method*

In a fixed reference frame, $(O, \hat{x}, \hat{y})$, the linear stability of a parallel mean flow $(\boldsymbol{U}_0, P_0, \rho_0)$ where:

$$\boldsymbol{U}_0(y) = U_0(y)\hat{x}, \qquad U_0(y) = \frac{1}{1+\sinh(y)^{2n}},$$

$$\rho_0(y) = 1 + (s-1)U_0(y), \qquad s = \frac{\rho_0(0)}{\rho_0(\infty)} = \rho_0(0),$$

$$P_0(y) = P_0 = \text{Const},$$

is studied. This basic flow is a two-parameter, (s, n), family of variable-density incompressible plane jets (see figure 1). This family is a solution of the stationary incompressible and inviscid Euler equations (it is well known that viscosity has only a dumping effect regarding linear growth rates in the present case (Drazin & Reid 1982)). In these formulae, s is the density ratio of the jet to ambient fluid and n is used to control smoothly the thickness of the jet shear layer. (Indeed, the momentum thickness of the velocity profile is $\theta(n) = \int_0^\infty U_0(1-U_0)\,\mathrm{d}y \simeq 0.33/n$ and the vorticity thickness is $\delta_\omega(n) = (U_0(0) - U_0(\infty))\max(1/(\mathrm{d}U_0/\mathrm{d}y)) \simeq 1.3/n$.) For $n = 1$, we recover the Bickley jet (the $\mathrm{sech}^2(y)$ velocity profile) and for $n = \infty$ the top-hat profile. These profiles were introduced, in a slightly different form, and studied by Yu & Monkewitz (1990).

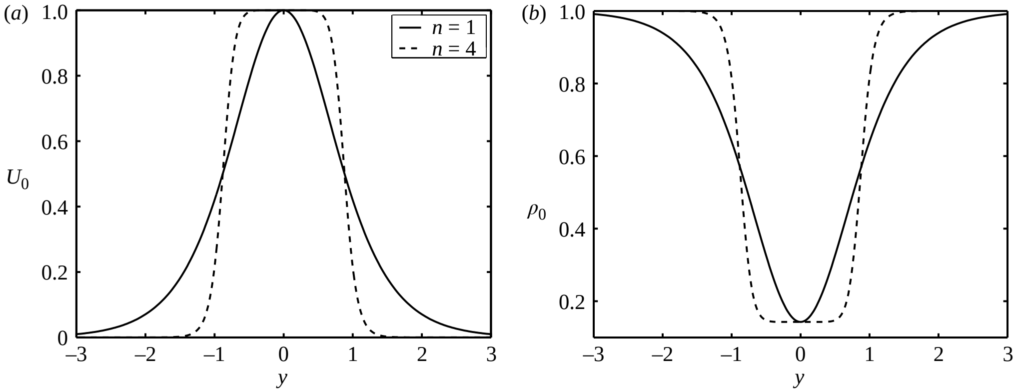

FIGURE 1. (*a*) Velocity and (*b*) density profiles of the basic flow for different values of n and for $s = 1/7$.

Superposing a perturbation flow (u, v, p, ρ) onto the mean one, the linear Euler equations around the basic flow read:

$$\frac{\partial u}{\partial t} + U_0 \frac{\partial u}{\partial x} + v U_0' = -\frac{1}{\rho_0}\frac{\partial p}{\partial x}, \tag{3.1}$$

$$\frac{\partial v}{\partial t} + U_0 \frac{\partial v}{\partial x} = -\frac{1}{\rho_0}\frac{\partial p}{\partial y}, \tag{3.2}$$

$$\frac{\partial u}{\partial x} + \frac{\partial v}{\partial y} = 0, \tag{3.3}$$

where the prime denotes y derivative and where the equation for ρ is dropped because it is only an advection by (u, v).

Looking for normal mode solutions:

$$\Phi(x, y, t) \mapsto \Phi(y) \exp(\mathrm{i}(kx - \omega t)),$$

with Φ any component of the perturbation flow, the equations for the perturbations become:

$$-\mathrm{i}\omega u + U_0 \mathrm{i}ku + vU_0' = -\frac{1}{\rho_0}\mathrm{i}kp, \tag{3.4}$$

$$-\mathrm{i}\omega v + U_0 \mathrm{i}kv = -\frac{1}{\rho_0}p', \tag{3.5}$$

$$\mathrm{i}ku + v' = 0. \tag{3.6}$$

Eliminating u and v from these equations and using the fact that perturbations vanish at infinity lead to a differential eigenvalue problem for the pressure:

$$p'' - \left(\frac{\rho_0'}{\rho_0} + 2\frac{U_0'}{U_0 - c}\right)p' - k^2 p = 0, \tag{3.7}$$

$$c = \omega/k, \tag{3.8}$$

$$p(\pm\infty) = 0. \tag{3.9}$$

It is well known that this problem admits two independent eigenfunction solutions: the varicose mode (p symmetric (with respect to y), u symmetric and v antisymmetric) and the sinuous mode (p antisymmetric, u antisymmetric and v symmetric).

The above pressure eigenvalue problem can be solved analytically only when $n = \infty$ (top-hat profiles). In this case, it is found that the varicose mode first becomes absolutely unstable at $s = s_{ca} = 0.79$ and that the sinuous mode transits at $s = s_{ca} = 0.29$ (Yu & Monkewitz 1990). For finite values of n, the problem must be numerically treated, however. To do so, the second-order differential equation is transformed to a set of two first-order ones. The symmetry of this initial-value problem depends on boundary conditions and the problem is solved by the shooting method for the complex eigenvalues $c = c_r + \mathrm{i}c_i$. The boundary conditions are:

(i) $p(0) = 1,\ p'(0) = 0,\ p(y \to \infty) \sim \exp(-ky),\ p'(y \to \infty) \sim -k\exp(-ky)$ for the varicose mode.

(ii) $p(0) = 0,\ p'(0) = 1,\ p(y \to \infty) \sim \exp(-ky),\ p'(y \to \infty) \sim -k\exp(-ky)$ for the sinuous mode.

The shooting method is precise but local in nature in the c plane. So, we must make a good initial guess for the method to converge. To overcome this difficulty, a global method based on matrix diagonalization is also used. In the temporal stability case ($k \in \mathbb{R}$ given, $\omega \in \mathbb{C}$ unknown) using the Chebyshev spectral collocation method with the mapping:

$$y = \tan\left(\tfrac{1}{2}\pi\xi\right), \qquad \xi \in [-1, 1],$$

equation (3.7) is transformed to a generalized eigenvalue problem:

$$Ap = cBp, \tag{3.10}$$

$$A = U_0 D^{(2)} - (2U_0' + (\rho_0'/\rho_0)U_0)D^{(1)} - k^2 U_0 D^{(0)}, \tag{3.11}$$

$$B = D^{(2)} - (\rho_0'/\rho_0)D^{(1)} - k^2 D^{(0)}, \tag{3.12}$$

where $D^{(2)}$, $D^{(1)}$ and $D^{(0)}$ are the order two, one and zero (the identity matrix) spectral differentiation matrices, respectively, compatible with the boundary conditions (3.9).

In the spatial stability case ($k \in \mathbb{C}$ unknown, $\omega \in \mathbb{R}$ given), however, k appears nonlinearly in equation (3.7) and it is better to proceed otherwise. The linearized Euler equations are written in the following way:

$$\frac{\partial}{\partial x}\begin{pmatrix} u \\ v \\ p \end{pmatrix} = \begin{pmatrix} 0 & -D^{(1)} & 0 \\ 0 & (\mathrm{i}\omega/U_0)D^{(0)} & -1/(\rho_0 U_0)D^{(1)} \\ (\rho_0 \mathrm{i}\omega)D^{(0)} & \rho_0\left(U_0 D^{(1)} - U_0' D^{(0)}\right) & 0 \end{pmatrix}\begin{pmatrix} u \\ v \\ p \end{pmatrix}$$

and the spatial eigenvalues are those of the matrix appearing in the right-hand side.

The difficulty with the global diagonalization method is the number of eigenvalues returned: if M is the number of Chebychev polynomials used, M eigenvalues are obtained in the temporal case and $3M$ in the spatial case. The spurious ones are characterized by a high number of oscillations of the corresponding eigenfunctions. So, to select the good candidates as the initial guess for the shooting method, the number of maxima of each eigenfunction are automatically counted and only those with fewer than four maxima in $[-1, 1]$ are retained.

3.2. *Results*

A check of the above described procedures is reported in figure 2. For $n = 1$ and $s = 1$, the same temporal and spatial growth rates, for the varicose and the sinuous modes, as those published in Mattingly & Criminale (1971) and Drazin & Reid (1982) are retrieved. Note also the good agreement of the shooting and diagonalization methods. Furthermore, this figure clearly shows that the sinuous mode dominates the varicose one, in a linear evolution for the uniform density Bickley jet case, since it has a higher

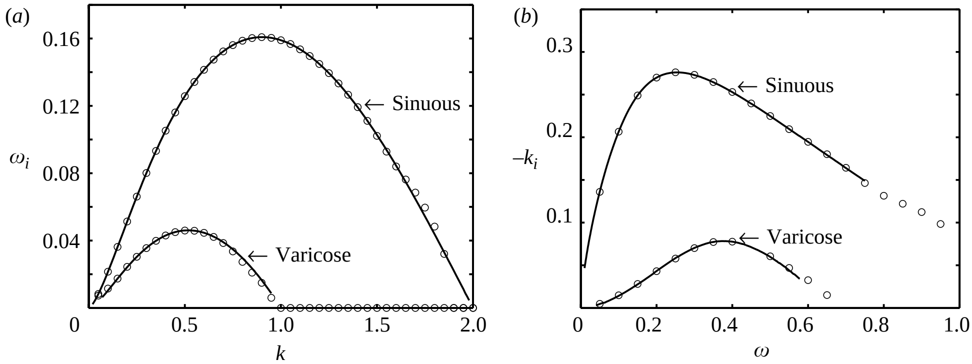

FIGURE 2. (*a*) Temporal and (*b*) spatial dispersion relations obtained from ——, the shooting and ○, diagonalization methods. Note the good agreement of the two methods and that the sinuous mode is more unstable than the varicose one for $n = 1$ and $s = 1$.

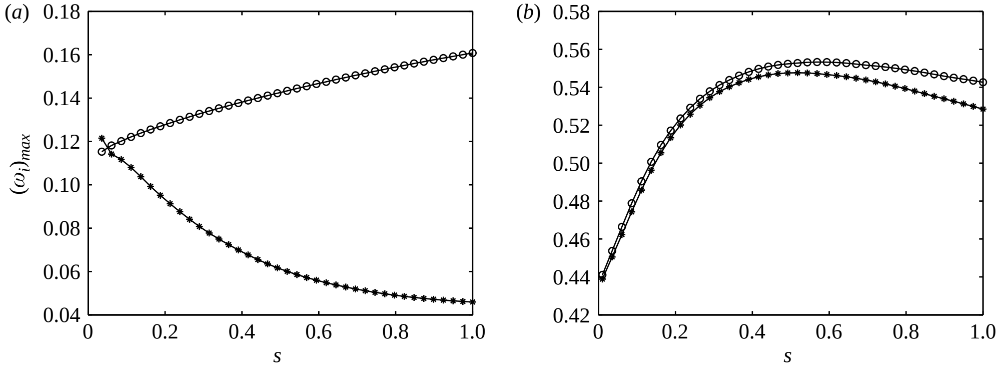

FIGURE 3. Maximum temporal growth rate $(\omega_i)_{max}$ as a function of the density ratio s for (*a*) $n = 1$ and (*b*) $n = 4$. Note that as s decreases, the varicose mode (●) becomes as important as the sinuous mode (○) especially for the top-hat-like profile ($n = 4$).

maximum growth rate. This feature does not remain the same when the density ratio decreases or n increases: the maximum growth rate of the varicose mode can have the same or a higher magnitude than that of the sinuous one (see figures 3 to 7). This suggests, depending on the values of the parameters s and n, that the varicose and sinuous modes can coexist and that the varicose mode can dominate in a linear evolution.

Spatial dispersion relations also show that only the varicose mode is subject to a convective–absolute transition for $s \in [0.1, 1]$ and $n \in \{1, 4\}$. Two spatial branches ‘pinch’ (Huerre & Monkewitz 1985) at $0.14 \leqslant s_{ca} < 0.15$ for $n = 1$ (figure 5) and at $0.93 \leqslant s_{ca} < 0.94$ for $n = 4$ (figure 7). Note that just before the transition, for $n = 1$, the maximum spatial growth rate is 0.38 at $s = 0.15$ for the varicose mode which is greater than 0.28, the corresponding maximum spatial growth rate of the sinuous mode at the same s. The same thing occurs for $n = 4$ with a maximum spatial growth rate of 1.29 at $s = 0.94$ for the varicose mode and 1.18 for the sinuous mode at the same value of s. Therefore, a natural question is: does the convective/absolute transition dictate its frequency to the nonlinear evolution of the jet, leading to a global oscillating varicose mode, or is it, simply, the frequency of the maximum varicose growth rate that does? This question is addressed in the following section.

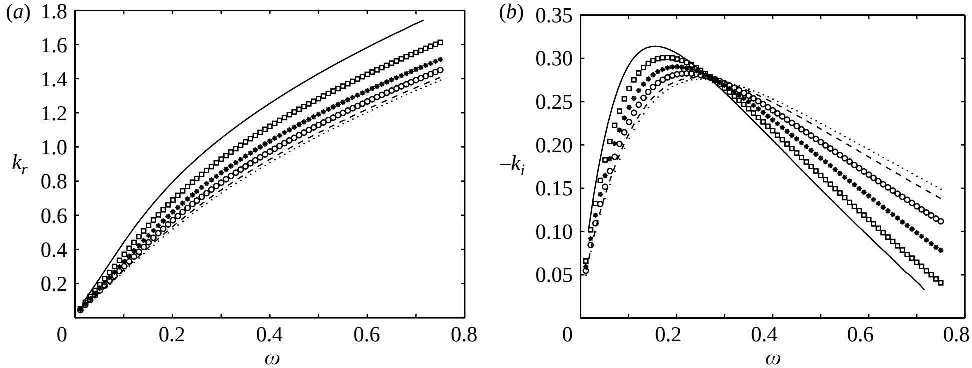

FIGURE 4. Spatial dispersion relations of the sinuous mode of the Bickley jet for $s \in [0.1, 1]$, $n = 1$. Note the weak dependency of the maximum growth rate on s and the absence of convective absolute transition for those values of s. ·, $s = 1$; - - -, 0.9; ○, 0.7; ●, 0.5; □, 0.3; ——, 0.1.

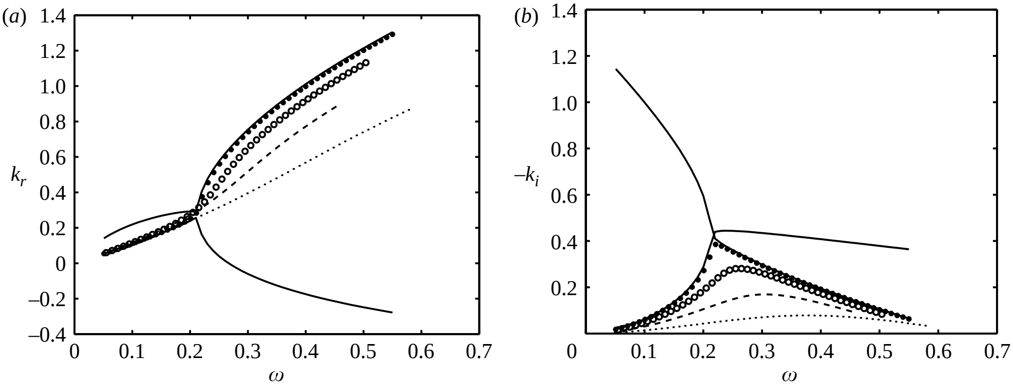

FIGURE 5. Spatial dispersion relations of the varicose mode of the Bickley jet for $s \in [0.14, 1]$, $n = 1$. Note the strong dependency of the maximum growth rate on s and the convective/absolute transition that occurs at $0.14 \leqslant s_{ca} < 0.15$. ·, $s = 1$; - - -, 0.4; ○, 0.22; ●, 0.15; ——, 0.14.

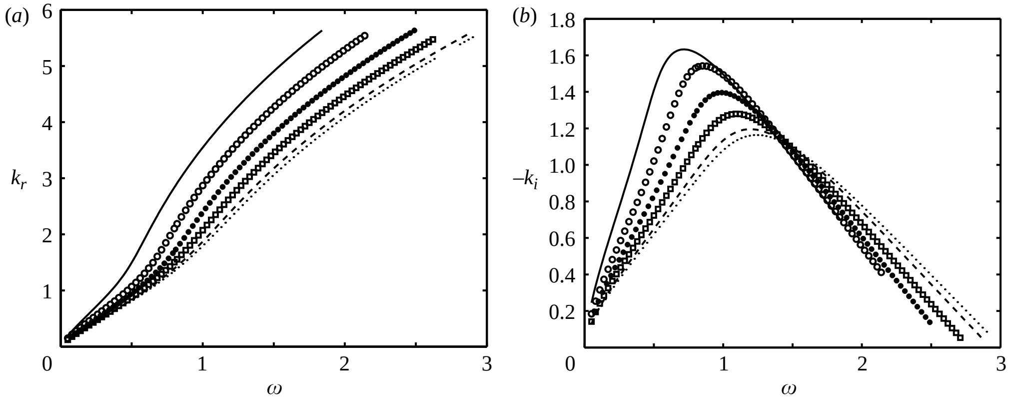

FIGURE 6. Spatial dispersion relations of the sinuous mode of the top-hat-like jet for $s \in [0.1, 1]$, $n = 4$. Note the absence of convective/absolute transition for those values of s. Key as figure 4.

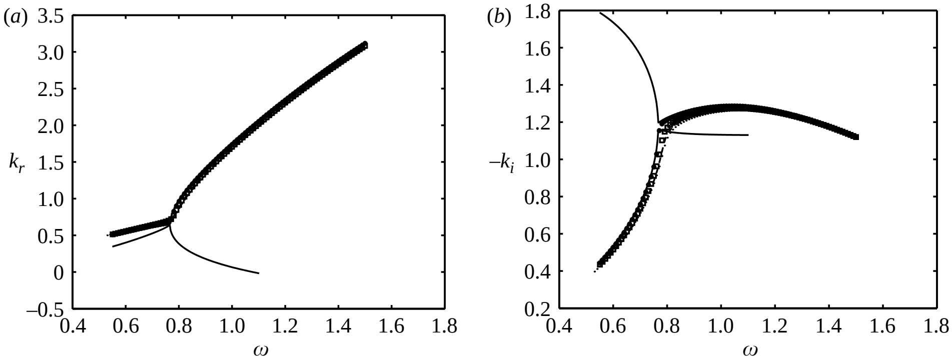

FIGURE 7. Spatial dispersion relations of the varicose mode of the top-hat-like jet for $s \in [0.93, 1]$, $n = 4$. Note the convective/absolute transition that occurs at $0.93 \leqslant s_{ca} < 0.94$. •, $s = 1$; - - -, 0.99; □, 0.97; ●, 0.94; ——, 0.93.

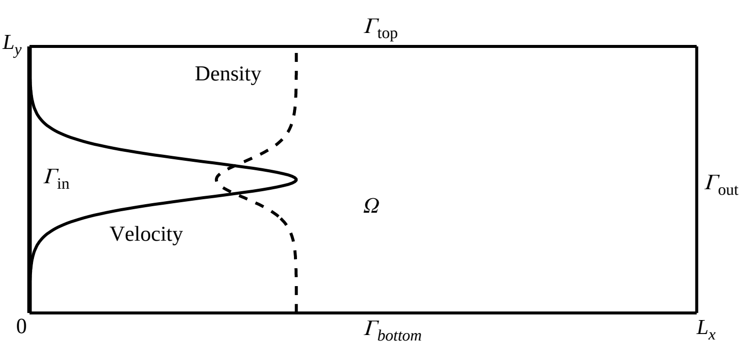

FIGURE 8. Geometry of the computational domain. Note that for artistic considerations, the real scale is not respected in this figure, especially the vertical one.

4. Nonlinear study

4.1. *Calculation domain*

Equations (2.2) are solved numerically in a rectangular domain $\Omega = [0, L_x] \times [0, L_y]$ with boundary $\partial\Omega = \Gamma_{in} \cup \Gamma_{out} \cup \Gamma_{bottom} \cup \Gamma_{top}$. The geometry of the problem is presented in figure 8. The grid mesh is uniform in the x- and y-directions and the steps are noted h_x and h_y, respectively. For convenience considerations, see §4.5, the same odd number, N, of mesh points is used in both directions. The runs are performed on a conventional PC with $N = 129$, 257 or 513.

4.2. *Numerical equations*

Let n superscript denote the time step at which a variable is calculated and Δt the time step. A standard time-splitting projection method in two steps (see for example Boersma, Brethouwer & Nieuwstadt 1998) is used to solve (2.2). To outline simply this way to proceed, the simple Euler temporal scheme is used even if another temporal discretization method (see below) is actually used. We first evaluate, from the actual velocity $\boldsymbol{v}^n$ and density ρ^n, an intermediate velocity field $\boldsymbol{v}^*$ solution of:

$$\frac{\boldsymbol{v}^* - \boldsymbol{v}^n}{\Delta t} = -(\boldsymbol{v}^n \cdot \nabla)\boldsymbol{v}^n + \frac{1}{\rho^n}\frac{1}{Re}\Delta \boldsymbol{v}^n.$$

Obviously, $\boldsymbol{v}^*$ is not a divergence-free field. Then, a Poisson-like equation is used to enforce the incompressibility in the numerical simulation. This equation can easily be obtained through the divergence operator applied to the momentum equation:

$$\nabla \cdot \left(\frac{1}{\rho^n} \nabla p \right) = \frac{1}{\Delta t} \nabla \cdot \boldsymbol{v}^*. \tag{4.1}$$

Note the main difference between (4.1) and a Poisson equation ($\Delta\varphi = f$): the operator is not the isotropic Laplacian, but an anisotropic operator which mixes pressure and density. Finally, the new velocity $\boldsymbol{v}^{n+1}$ is calculated with:

$$\boldsymbol{v}^{n+1} = \boldsymbol{v}^* - \frac{1}{\rho^n} \nabla p \ \Delta t. \tag{4.2}$$

If $\boldsymbol{v} = (u, v)$, all the procedure and previous equations can be summed up as follows:

$$\left.\begin{aligned}
&\frac{u^* - u^n}{\Delta t} = -\left(u^n \frac{\partial}{\partial x} + v^n \frac{\partial}{\partial y} \right) u^n + \frac{1}{Re} \frac{1}{\rho^n} \left(\frac{\partial^2 u^n}{\partial x^2} + \frac{\partial^2 u^n}{\partial y^2} \right), \\
&\frac{v^* - v^n}{\Delta t} = -\left(u^n \frac{\partial}{\partial x} + v^n \frac{\partial}{\partial y} \right) v^n + \frac{1}{Re} \frac{1}{\rho^n} \left(\frac{\partial^2 v^n}{\partial x^2} + \frac{\partial^2 v^n}{\partial y^2} \right), \\
&\nabla \cdot \left(\frac{1}{\rho^n} \begin{pmatrix} \partial p/\partial x \\ \partial p/\partial y \end{pmatrix} \right) = \frac{1}{\Delta t} \nabla \cdot \begin{pmatrix} u^* \\ v^* \end{pmatrix}, \\
&u^{n+1} = u^* - \frac{1}{\rho^n} \frac{\partial p}{\partial x} \Delta t, \qquad v^{n+1} = v^* - \frac{1}{\rho^n} \frac{\partial p}{\partial y} \Delta t, \\
&\frac{\rho^{n+1} - \rho^n}{\Delta t} + \left(u^n \frac{\partial}{\partial x} + v^n \frac{\partial}{\partial y} \right) \rho^n = 0.
\end{aligned}\right\} \tag{4.3}$$

4.3. *Temporal discretization*

A third-order Runge–Kutta discretization scheme to perform the temporal discretization is chosen. It is an explicit scheme. Thus, to integrate $\partial a/\partial t = f(a, x, y, t)$ for $t \in [0, T]$, the following quantities are successively evaluated: $d_1 = \Delta t\ f(a^n, x, y, t)$, then $d_2 = \Delta t\ f(a^n + d_1/3, x, y, t)$ and finally $d_3 = \Delta t\ f(a^n + 2d_2/3, x, y, t)$. Then, we have:

$$a^{n+1} = a^n + \tfrac{1}{4}(d_1 + 3\,d_3).$$

Such a scheme provides good stability and is not too expensive in calculating time. The time step is given by a CFL condition:

$$\Delta t = \beta \, \frac{\min(h_x, h_y)}{\max(u(t = 0))},$$

where β is a safety coefficient that is less than 1 for stability reasons. For the runs shown here, $\beta = 0.5$.

4.4. *Spatial discretization*

For the spatial discretization, finite-difference schemes are used:

(i) centred in the inner of the computation domain,

(ii) not centred, but second-order accurate on the borders.

Special attention is paid to border formulae since the lowest order in the domain limits the global order for all the simulations. Details are given in Appendix A.

4.5. *Solution of the pressure equation*

To solve the linear elliptic equation of the pressure with appropriate boundary conditions:

$$\nabla\cdot\left(\frac{1}{\rho}\nabla p\right)=\nabla\cdot\left(\frac{\boldsymbol{v}^{\star}}{\Delta t}\right)\quad \text{in}\quad \Omega, \tag{4.4}$$

$$B(p)=0\quad \text{in}\quad \partial\Omega, \tag{4.5}$$

which is more complicated than the Poisson equation, that would be obtained for a homogeneous fluid, a multigrid method is used. This method presents the advantage of solving the equations (4.4) and (4.5), discretized on N^2 two-dimensional grid points, in $O(N^2\log(N))$ operations, which is comparable to fast Fourier transform (FFT) based methods. Details are given in Appendix B.

4.6. *Boundary conditions*

The fact that this part requires fine tuning to obtain accurate results in a direct simulation is underlined. Several methods were tried and most of them did not work in the present study.

4.6.1. *Inflow*

At the inlet Γ_{in}, the entrance velocity and density profiles are simply enforced using the basic profiles presented in the linear study:

$$u(0,y,t)=U_0(y),\qquad U_0(y)=\frac{1}{1+\sinh(y)^{2n}},$$

$$\rho(0,y,t)=\rho_0(y)=1+(s-1)U_0(y),\qquad s=\frac{\rho_0(0)}{\rho_0(\infty)}=\rho_0(0),$$

whereas the transverse velocity $v(0,y,t)$ is set to zero.

In these simulations, two profiles are mainly used (figure 1):

(i) $n=1$: this is the sech^2 profile also called Bickley jet. The velocity gradients are moderate and this profile allows low-resolution runs ($N\geqslant 129$);

(ii) $n=4$: this is what is called, herein, a 'top-hat-like' profile since it has a nearly zero gradient part in the centre whereas the lateral gradients are large but finite. The stiffness is anyhow larger than in the Bickley jet. To obtain accurate results, higher resolution ($N\geqslant 257$) is required.

Apart from this boundary condition, the other ones (outflow and lateral conditions) are not physical: they are required because of the finite size of the simulation domain. Ideal boundary conditions do not exist: whatever you do, you obtain perturbations on your results inside the domain. Good boundary conditions are compromises between what you want (let the fluid out) and corollary effects you do not want (perturbations inside the calculation domain).

4.6.2. *Outflow*

The main difficulty of the outflow condition is that it should let the fluid leave the calculation domain without any rebound effect (see Givoli 1991; Gresho 1991 for a review). Several outlet boundary conditions on Γ_{out} were tried. The free shear stress condition, $\partial u/\partial y+\partial v/\partial x=0$, induces spurious reflection and increases the divergence of the velocity field inside the domain. Free advection condition:

$$\frac{\partial\psi}{\partial t}+\alpha\frac{\partial\psi}{\partial x}=0\quad\text{with}\quad \alpha=\begin{cases}u(L_x,y,t) & \text{if } u(L_x,y,t)>0,\\ 0 & \text{otherwise,}\end{cases}$$

where ψ represents any base quantity, is unable to maintain the velocity divergence at low values inside the domain: the divergence increases until calculation explodes. The main problem of this boundary condition is that if $u < 0$ somewhere on the border, the excess of a accumulates and is not advected downstream. In the usual convection condition, used for example by Boersma *et al.* (1998), α is the mean velocity over the outflow boundary; this condition does not provide good results since it artificially increases the jet width.

Finally, a null normal velocity derivative is imposed:

$$\frac{\partial \boldsymbol{v}}{\partial x}(L_x, y) = \mathbf{0}, \quad y \in \Gamma_{out}.$$

This is the best compromise of all other methods used before.

4.6.3. *Lateral conditions*

On lateral limits $\Gamma_{bottom} \cup \Gamma_{top}$, boundary conditions should not suck up the fluid. Practically, the normal derivatives of the longitudinal velocity and the value of the normal velocity are set to zero:

$$\frac{\partial u}{\partial y}(x,0) = \frac{\partial u}{\partial y}(x, L_y) = 0, \quad v(x,0) = v(x, L_y) = 0, \quad x \in [0, L_x].$$

As a consequence, such boundary conditions reduce the deviation possibility for the jet: it gives priority to the downstream direction.

Nevertheless, this is not a perfect solution since, if the jet spreads enough to become close to these limits, a rebound effect can occur. Another solution is to use a lateral damping function. This is easy to implement and is widely used in direct numerical simulation (see for example Slinn & Riley 1998; Bhaganagar, Rempfer & Lumley 2000; Stanley, Sarkar & Mellado 2002) but it reduces the physical calculation domain and it is not used in the present work.

4.7. *Flux correction*

The projection (4.1) associated with the Neumann boundary condition requires another condition, with those mentioned before, to be compatible with divergence-free condition. Let us integrate (4.1) over the calculation domain and use Ostrogradski's theorem:

$$\oint_{\partial\Omega} \frac{1}{\rho}\nabla p \cdot \boldsymbol{n}\, \mathrm{d}\ell = -\frac{1}{\Delta t}\oint_{\partial\Omega} \boldsymbol{v}^* \cdot \boldsymbol{n}\, \mathrm{d}\ell.$$

Since the normal derivative of the pressure is supposed to be zero, the right-hand side of this equation must be zero as well. This means that the sum of the normal velocity on the limit of the domain must vanish. Up to now, no such condition is enforced to the velocity field. Indeed, the pressure equation (4.1) is solved, to enforce a divergence-free velocity field, inside the calculation domain and not on its boundaries. To do so, let F denote the total flux:

$$\int_{\Omega} \boldsymbol{v}^* \cdot \boldsymbol{n} \mathrm{d}\ell = -\int_{\Gamma_{in}} u^* \mathrm{d}y + \int_{\Gamma_{out}} u^* \mathrm{d}y = F. \tag{4.6}$$

Then, using any function, r, the equation

$$-\int_{\Gamma_{in}} u^*(y)\mathrm{d}y + \int_{\Gamma_{out}} \left(u^*(y) - \frac{F r(y)}{\displaystyle\int_{\Gamma_{out}} r(y)\mathrm{d}y} \right) \mathrm{d}y = 0, \tag{4.7}$$

is exactly verified. When the jet goes through the calculation domain, the sum of the outflow is approximately equal to the sum of the inflow and thus F is small. To ensure that the total velocity flux is null, we may use a corrected value of the velocity at the outflow boundary given by:

$$u^*_{\Gamma_{out}}(y) - FR(y), \quad R(y) = \frac{r(y)}{\displaystyle\int_{\Gamma_{out}} r(y)\mathrm{d}y}, \quad y \in \Gamma_{out}. \tag{4.8}$$

Using the discrete grid notations and a Gaussian function for r, a 'repartition function' R is defined:

$$R(\alpha_i) = \frac{\exp(-(\alpha_i/D)^2)}{\displaystyle\sum_{m=0}^{N-1} \exp(-(\alpha_m/D)^2)} \quad \text{with} \quad \alpha_i = y_i - \tfrac{1}{2}L_y, \tag{4.9}$$

where D is the diameter of this Gaussian function and $y_i = ih_y$ for some integer i between 0 and $N-1$. Then $u^*(L_x, y_i)$ (longitudinal velocity at the outflow boundary) is incremented with a small velocity component:

$$u^*(L_x, y_i) \longleftarrow u^*(L_x, y_i) + \sum_{m=0}^{N-1}(u^*(0, y_m) - u^*(L_x, y_m))R(\alpha_i). \tag{4.10}$$

This ensures that the total velocity flux is null. The choice of a Gaussian function, for r, is somewhat arbitrary. It will be shown, in the next sections, that this choice and the correction of the outflow velocity, using (4.10), does not spoil the frequencies of the physical problem under consideration.

4.8. *Tests and code validation*

4.8.1. *The linear approximation*

To test the numerical computations of the procedure described in the previous sections, § 4.1 to 4.7, the linear impulse response of equations (4.3) on Ω is calculated and we try to recover the dispersion relations obtained by diagonalization and shooting methods in § 3. Thus, equation (4.3) is linearized around the mean parallel variable-density flow $(\boldsymbol{U_0}, P_0, \rho_0)$, given in § 3, which is supposed to be a steady solution of the Navier–Stokes equations (of course this is true for $Re = \infty$). The velocity in the downstream direction is denoted $U_0 + u$, in the spread direction v and the density is $\rho_0 + \rho$. Equations (4.3) can then be rewritten at leading order in (u, v, ρ):

$$\left.\begin{aligned}
&\frac{u^* - u^n}{\Delta t} = -U_0\frac{\partial u^n}{\partial x} - v^n\frac{\mathrm{d}U_0}{\mathrm{d}y} + \frac{1}{Re}\frac{1}{\rho_0}\left(\frac{\partial^2 u^n}{\partial x^2} + \frac{\partial^2 u^n}{\partial y^2} - \frac{\rho^n}{\rho_0}\frac{\mathrm{d}^2 U_0}{\mathrm{d}y^2}\right),\\
&\frac{v^* - v^n}{\Delta t} = -U_0\frac{\partial v^n}{\partial x} + \frac{1}{Re}\frac{1}{\rho_0}\left(\frac{\partial^2 v^n}{\partial x^2} + \frac{\partial^2 v^n}{\partial y^2}\right),\\
&\nabla\cdot\left(\frac{1}{\rho_0}\begin{pmatrix}\partial p/\partial x\\ \partial p/\partial y\end{pmatrix}\right) = \frac{1}{\Delta t}\nabla\cdot\begin{pmatrix}u^*\\ v^*\end{pmatrix},\\
&u^{n+1} = u^* - \frac{1}{\rho_0}\frac{\partial p}{\partial x}\Delta t, \ v^{n+1} = v^* - \frac{1}{\rho_0}\frac{\partial p}{\partial y}\Delta t,\\
&\frac{\rho^{n+1} - \rho^n}{\Delta t} + \left(u^n\frac{\partial}{\partial x} + v^n\frac{\partial}{\partial y}\right)\rho_0 + U_0\frac{\partial \rho^n}{\partial x} = 0.
\end{aligned}\right\} \tag{4.11}$$

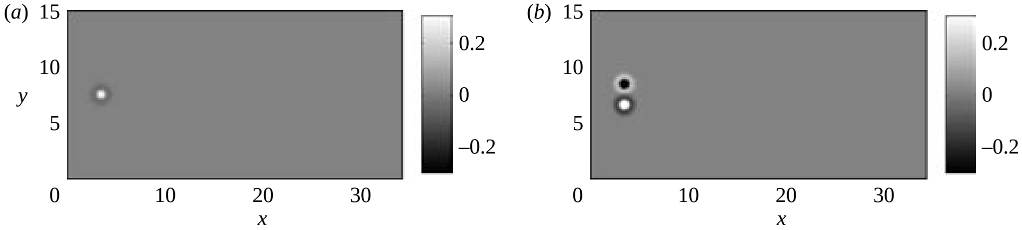

FIGURE 9. Initial vorticity condition used to obtain the impulse response of (*a*) the sinuous and (*b*) the varicose mode.

Since there are two main instability modes:

(i) the sinuous mode with y antisymmetric longitudinal velocity,

(ii) and the varicose mode with y symmetric longitudinal velocity,

different Gaussian perturbations, that mimic the Dirac δ function, are used as initial conditions to excite each mode (see figure 9). To obtain the sinuous mode, the Gaussian perturbation is centred on $(x_1, y_1 = L_y/2)$ where x_1 is near the entrance. The following expressions are retained at $t = 0$ (see for example Delbende, Chomaz & Huerre 1998):

$$\left.\begin{aligned} u(x,y,0) &= -\epsilon\,\frac{y-y_1}{a}\;\mathrm{e}^{-((x-x_1)/a)^2}\;\mathrm{e}^{-((y-y_1)/a)^2},\\ v(x,y,0) &= \epsilon\,\frac{x-x_1}{a}\;\mathrm{e}^{-((x-x_1)/a)^2}\;\mathrm{e}^{-((y-y_1)/a)^2}, \end{aligned}\right\} \tag{4.12}$$

where a is the length scale of the perturbation, such that the δ function is recovered in the limit $a \rightarrow 0$, and ϵ is the small amplitude of the perturbation. For the varicose mode, two identical Gaussian perturbations which are symmetrically arranged and superposed at the same x_1 position are used:

$$\left.\begin{aligned} u(x,y,0) &= \epsilon\left(\frac{y-y_2}{a}\;\mathrm{e}^{-((y-y_2)/a)^2} - \frac{y-y_3}{a}\;\mathrm{e}^{-((y-y_3)/a)^2}\right)\mathrm{e}^{-((x-x_1)/a)^2},\\ v(x,y,0) &= \epsilon\,\frac{x-x_1}{a}\left(\mathrm{e}^{-((y-y_2)/a)^2} - \mathrm{e}^{-((y-y_3)/a)^2}\right)\mathrm{e}^{-((x-x_1)/a)^2}, \end{aligned}\right\} \tag{4.13}$$

where y_2 and y_3 are taken near the inflection points of the basic velocity profile. In the present calculations the values $\epsilon = 0.1$ and $a = 0.5$ are used.

These perturbations are divergence-free: this is important to avoid a spurious velocity field which could enter the calculation domain to compensate non-vanishing velocity divergence.

For each density ratio, the perturbation flow (only the perturbation is evaluated since the parallel flow remains undisturbed) is computed on a duration which is long enough to obtain the linear growth rate, but short enough to avoid nonlinear effects from the boundaries. An example of the Green functions obtained is reported in figure 10. After this, the linear temporal growth rate is calculated through a simplified Fourier analysis which leads to the results presented in the next paragraph.

4.8.2. *Linear analysis by direct numerical simulations*

Following Delbende *et al.* (1998), the Fourier method is used to analyse the results provided by direct numerical simulations in the linear approximation. The runs are 500 time steps long when $N = 129$ (with this duration, the initial perturbation is convected through the domain, but the nonlinear influence of the borders remains small). Analyses are performed on 50 of these 500 views of the flow (one each 10 time

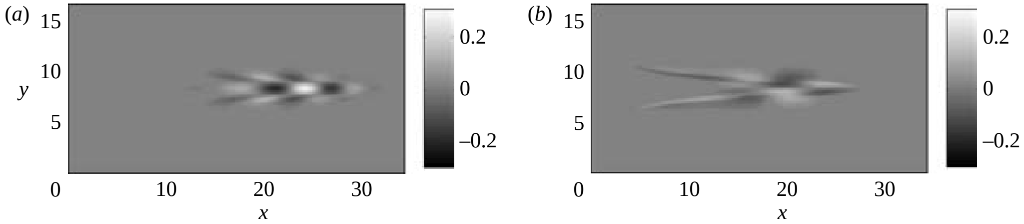

FIGURE 10. Green function of the vorticity of (a) the sinuous and (b) the varicose mode. These views are at the same time for $s = 1$.

steps). For greater resolution, 50 views are analysed as well, but the set is 1000 time steps long ($N = 257$) or 2000 ($N = 513$). Since the time step is divided by 2 when the resolution is increased by 2, all the analysed sequences have the same duration.

On each of the 50 records, a discrete Fourier transform in the x-direction is evaluated:

$$a_k(y,t) = \sum_x A(x,y,t)\,\exp(-\mathrm{i}\,k\,x 2\pi/L_x)\,,$$

where A is any physical base quantity (the vorticity is used). For a local linear growth, it is found that the scenario of the spatial expansion is self-similar in the y-direction so it is possible to use the mean value of each $a_k(y,t)$ in the y-direction:

$$\tilde{a}_k(t) = \frac{1}{N}\sum_y |a_k(y,t)|^2\,.$$

Following the linear analysis, the $\tilde{a}_k(t)$ should be given by:

$$\tilde{a}_k(t) = a_0 \exp(\sigma(k)\,t)\,.$$

To evaluate the exponential growth rate, two different times t_1 and t_2 ($t_2 > t_1$) are chosen and a logarithmic derivative to obtain the temporal dispersion relation is calculated:

$$\sigma(k) = \frac{\mathrm{d}\ln\tilde{a}_k}{\mathrm{d}t} \simeq \frac{\ln(\tilde{a}_k(t_2)) - \ln(\tilde{a}_k(t_1))}{t_2 - t_1}.$$

4.8.3. *Linear temporal growth rate*

The density ratio, s, is varied between 0.1 and 1. The growth rates of the sinuous mode are presented in figure 11. The maximum of each curve is not strongly affected by the density ratio (variations of $\sigma_{max} = \max_k(\sigma(k)) = \sigma(k_{max})$ and k_{max} are about 30% while the density ratio is divided by 10).

For the varicose mode, growth rates are shown in figure 12. Note that k_{max} is only slightly affected by the density ratio (36% variations) compared to the corresponding growth rate which increases (200% variations) when the density ratio decreases.

This evolution is different from the sinuous one since in that case, the growth rate decreases with the density ratio. As a consequence, the most unstable mode is the sinuous mode for density ratio above 0.2, but both modes are practically of the same importance if s is close to 0.1. Thus, both modes should grow for low density ratio. Compared with the linear analysis of § 3, the results of the present calculations are good and the agreement is better, as it should be, if the resolution is increased as shown on figure 13 (varicose mode). Note that the direct numerical calculations

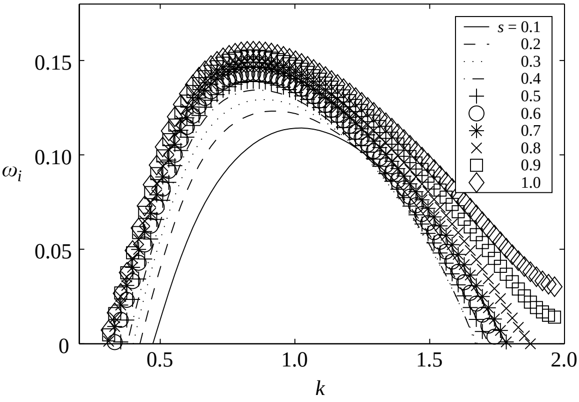

FIGURE 11. Temporal growth rate ω_i of the sinuous mode for various density ratios s.

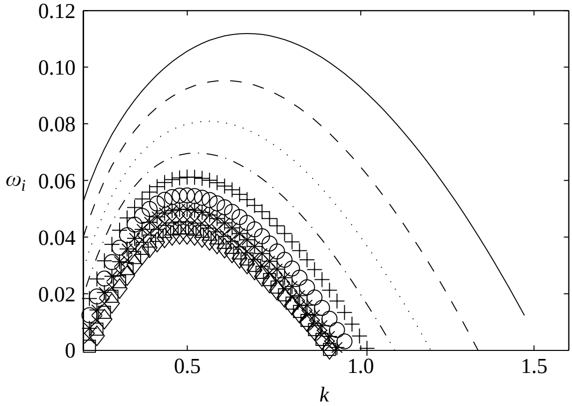

FIGURE 12. Temporal growth rate ω_i of the varicose mode for various density ratios s. Key as figure 11.

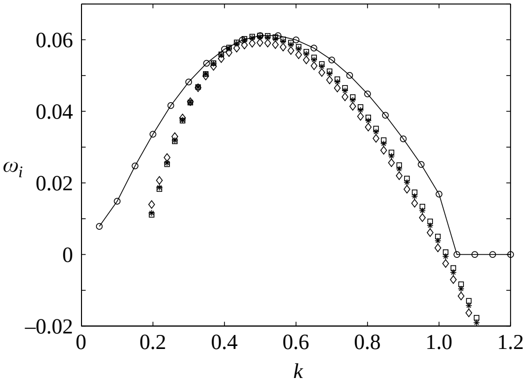

FIGURE 13. Comparison of temporal growth rate of the varicose mode, calculated with the linear analysis, and that obtained by direct simulation of the linearized Navier–Stokes equations for $s = 0.5$. Note that in numerical solutions the wavenumbers beyond the inviscid instability neutral mode are damped as it should be. ◇, DNS 128; *, DNS 256; □, DNS 512; ○, shooting and diagonalization.

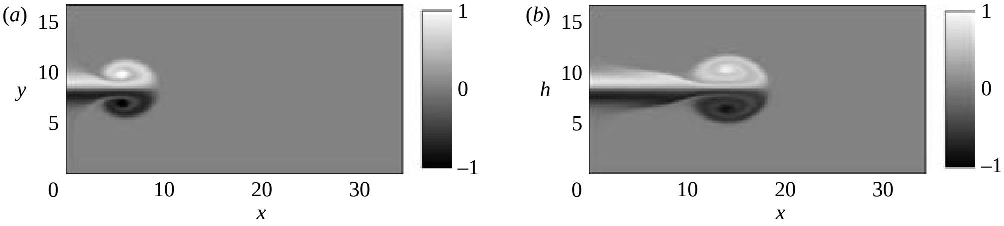

FIGURE 14. Vorticity in the calculation domain after (*a*) 600 and (*b*) 1200 time steps in the case of an initialization on the entrance border ($s = 1$, $N = 257$).

capture the maximum of the dispersion relation quite well at a low resolution: the difference with the 'semi-analytical' calculations performed in § 3 is less than 3% with 129 points and negligible with 513 points.

Nevertheless, a 'perfect' agreement for the entire dispersion relation cannot be reached since hypotheses are different in both cases. Indeed, in the linear analysis performed in § 3, the calculation is over an infinite domain with a perfect zero-limit for the calculated eigen modes, whereas in the linear impulse response, obtained by direct simulation, the calculation domain is bounded. As a consequence, the results for small k (large wavelength) cannot be satisfactorily resolved. Furthermore, the study of § 3 is inviscid, whereas the direct simulation is performed with large but finite Reynolds number ($Re = 1000$ in the present computations). This point may explain the discrepancy for large k values for which the viscosity is active.

4.9. *First glance at a full nonlinear simulation*

The nonlinear equations (4.3) are now simulated using two kinds of initial conditions:

(i) A zero initial velocity and a uniform density on the calculation domain:

$$u(x, y, 0) = v(x, y, 0) = 0, \qquad \rho(x, y, 0) = 1 \quad \text{in} \quad \Omega;$$

(ii) The longitudinal velocity is initiated with the basic profile of § 3, for all x, and the transverse velocity, v, with zero. This leads to an initial parallel flow in the calculation domain:

$$u(x, y, 0) = U_0(y), \quad v(x, y, 0) = 0, \quad \rho(x, y, 0) = \rho_0(y) \quad \text{in} \quad \Omega.$$

Note that for both cases, the basic profile is not fixed in all the simulations and the jet is free to evolve in the computational domain, contrary to the works of Delbende *et al.* (1998) and Pier & Huerre (2001) on wakes.

In the first case, the first steps of the calculation are used to let the fluid go through the domain. In doing so, the two characteristic Kelvin–Helmholtz starting vortices are observed (see figure 14).

Similarly, in the second case, since the parallel flow is not an exact solution of the Navier–Stokes equations, the first time steps are used to adjust this flow to a solution (see figure 15). This case requires fewer time steps than the previous one. Therefore, it is mainly used to initiate the calculations. For example, after about 1000 time steps when $N = 129$, the calculated flow is a laminar solution of the Navier–Stokes equation. It can be seen in figure 16 that in such a case, the longitudinal velocity profiles are almost uniform in the calculation domain and the transverse profiles are relatively small in amplitude.

Nevertheless, the first method is interesting: it is a good test to check the validity of the boundary conditions. Since there is no gravity, and so no privileged direction, the

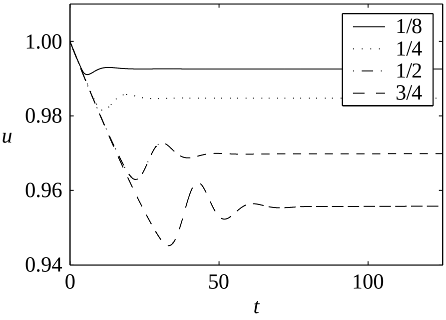

FIGURE 15. Axial velocity during first steps when initializing with a parallel flow ($s = 1$, $N = 257$, the first 4000 time steps are shown).

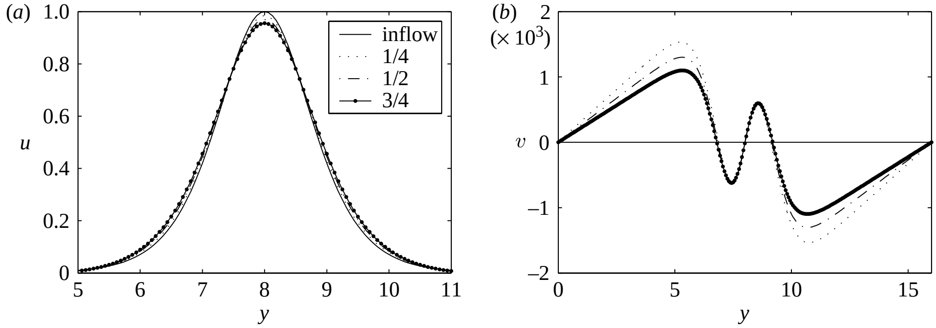

FIGURE 16. Velocity profiles at various positions after the initial disturbance has been convected out of the calculation domain: (*a*) longitudinal and (*b*) spanwise velocities ($s = 1$, $N = 257$, after 4000 time steps).

jet could, at least cost, turn to leave the calculation domain from the sides $\Gamma_{bottom} \cup \Gamma_{top}$ rather than going through the domain and leaving from Γ_{out}. Such a 'bad' behaviour is obtained when boundary conditions used at the outlet are not permeable enough.

After the laminar solution of the Navier–Stokes equation has been reached, truncation errors, although double-precision floating point is used, are sufficient to start an instability. The streamwise velocity is plotted, in the middle of the computational domain, against time in figure 17 and a frequency is measured: $\omega/(2\pi) = 0.35/(2\pi)$. It corresponds to the frequency of the most unstable sinuous mode (see § 3.2) in the spatial calculations (this is also a validation of the numerical computations in the nonlinear regime). Note that for the sinuous mode, no saturation state is found despite the fully nonlinear evolution. The amplitude of the oscillations increases until the jet touches the lateral sides for all L_y used.

4.10. *Nonlinear results*

A set of simulations for various density ratios and inflow profiles is performed. Let us study what occurs for the jet when the calculations are started with a parallel flow.

4.10.1. *The Bickley jet*

As stated in § 1, experimental observations show that the dynamics of plane jets change when the density ratio decreases. For high values of s, the sinuous mode is mainly observed whereas for low s, we observe the varicose mode. According to Yu & Monkewitz (1993), this behaviour occurs for a lower density ratio, s, than a critical

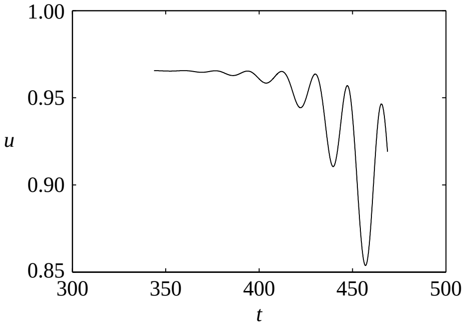

FIGURE 17. Axial velocity in the middle of the calculation domain after the establishment of the exact laminar solution of the Navier–Stokes equations (2000 time steps are shown, $s = 1$, $N = 129$).

one, s_{ca}, and is governed by the convective/absolute transition of the varicose mode (the sinuous mode does not show a transition).

Nevertheless, since the spatial linear growth rate of the varicose mode (see § 3.2) becomes greater than the sinuous one for lower s, before the transition occurs, this assumption should be made clearer, especially that the critical value, s_{ca}, found by Yu & Monkewitz, in their experimental work and linear instability analysis for an unbounded domain, is contested by the experimental work of Raynal *et al.* (1996). This is the main goal of the present section.

Before the convective/absolute transition ($s > s_{ca} \simeq 0.145$), the sinuous mode is the main mode and it is growing, as can be seen in figure 18. Lowering s, the jet ceases to touch lateral boundaries and becomes varicose consistently with the linear study. Around the transition, the behaviour of the jet is closer and closer to an oscillator. The initial perturbation, coming from the fact that initial conditions are exact solutions of Euler equations but not Navier–Stokes ones, produces more remnant oscillations than those in figure 15, but which also relax. The whole jet does not oscillate in a self-sustained manner for $s = 0.2$: closer to the inlet of the jet, oscillations vanish more quickly than those closer to the outlet (figure 19). Thus, this mode is global but not self-sustained. The angular frequency is $\omega \simeq 0.2$ at 3/4 of the calculation domain (figure 19*b*). It is in good agreement with the angular frequency of the spatial varicose mode having the maximum growth rate predicted by the linear theory (figure 5), but this is the angular frequency of the transition as well.

After the linearly predicted transition, the evolution is governed by the varicose mode. The initial perturbation excites several modes, but the Bickley jet responds with a single frequency. Nonlinear terms balance the linear growth rate. The main difference with a simulation close to the transition is that now a global mode is well installed; the same pure frequency can be observed at various stations in the flow (figure 20). This frequency is also observed far below the transition in agreement with Dee & Langer local marginal absolute instability criterion although the dynamics is fully nonlinear. A sequence of the varicose mode evolution in this case is given in figure 21. The main results of these computations are summed up in table 2.

Is this behaviour due to the convective/absolute transition as supposed by Yu & Monkewitz (1993)? The global oscillations observed are important for claiming that the transition is the key point to explain the change in the flow evolution. However, since, for the Bickley jet, the double root in k of the dispersion relation (the ‘pinching’), signalling the transition, occurs at the maximum of the linear growth rate curve, we

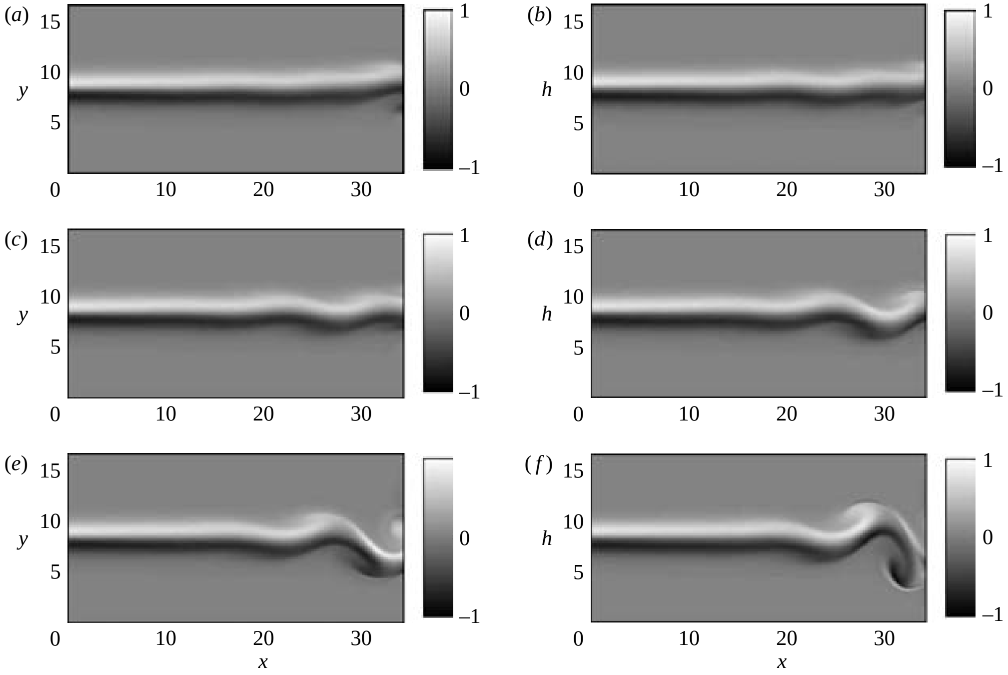

FIGURE 18. Sequence of a simulation before the convective/absolute transition (vorticity, $s = 0.3$, $N = 257$ and $n = 1$. Each view is separated by 300 time steps).

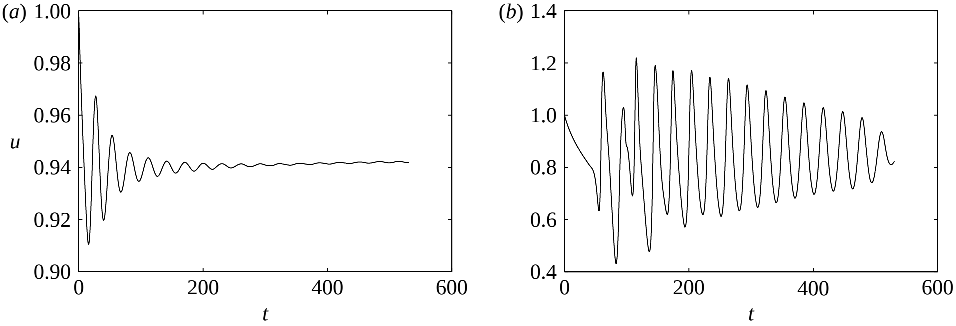

FIGURE 19. Downstream velocity at (a) 1/4 of the calculation domain and (b) at 3/4 ($s = 0.2$, $N = 257, n = 1$).

are still not totally sure: the global mode observed could be the resonance of the most amplified mode with the non-periodic boundary conditions used for example.

4.10.2. *The top-hat-like jet* ($n = 4$)

To show definitely that the convective/absolute transition explains the evolution of the flow for $s < s_{ca}$, simulations with a top-hat-like profile ($n = 4$ in the expression of U_0) are performed. The locations of the double root in k and of the maximum of the growth rate curve are well separated in this profile, as shown on figure 7: the maximum of the growth rate for $s \simeq s_{ca}$ is at an angular frequency about $\omega = 1.2$, whereas the location of the double root in k is at $\omega = 0.77$. This difference is large enough to find a clear answer to the question. However, as mentioned in § 4.6.1, such a profile is more difficult to simulate since it is stiffer. Therefore, the runs are done

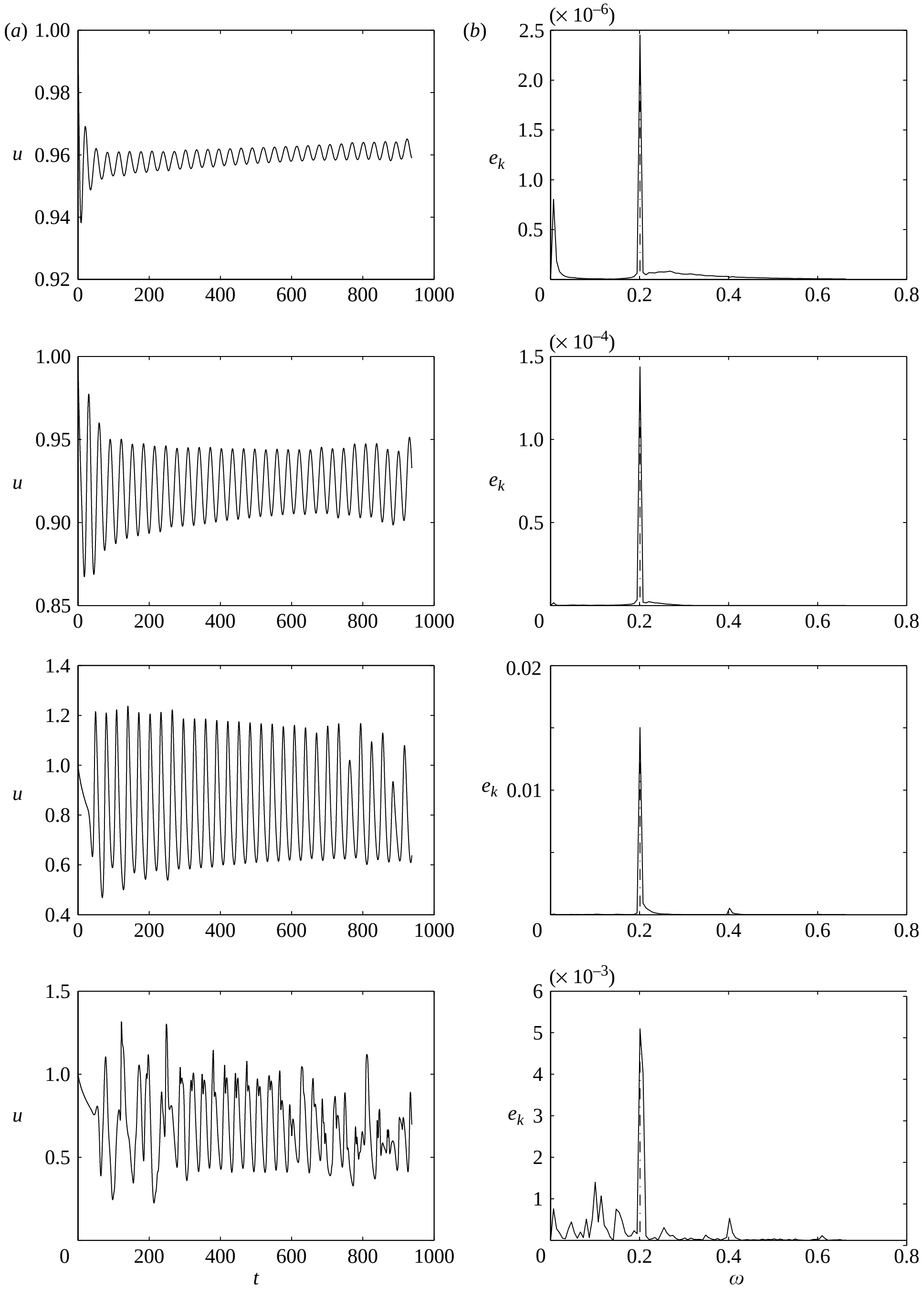

FIGURE 20. Global mode. From top to bottom, velocity u at 1/8, 1/4, 1/2, 3/4 of the computational domain for the Bickley jet. (*a*) $u(t)$; (*b*) the associated power spectrum $e_k(\omega)$ ($s = 0.13$, $n = 1$, $N = 257$, 30 000 time steps are shown). This is clearly a self-sustained oscillator behaviour at an angular frequency $\omega = 0.20$. The corresponding Strouhal number, defined by $S_t = 2f\bar{L}/\bar{U}$ is $S_t = 0.06$.

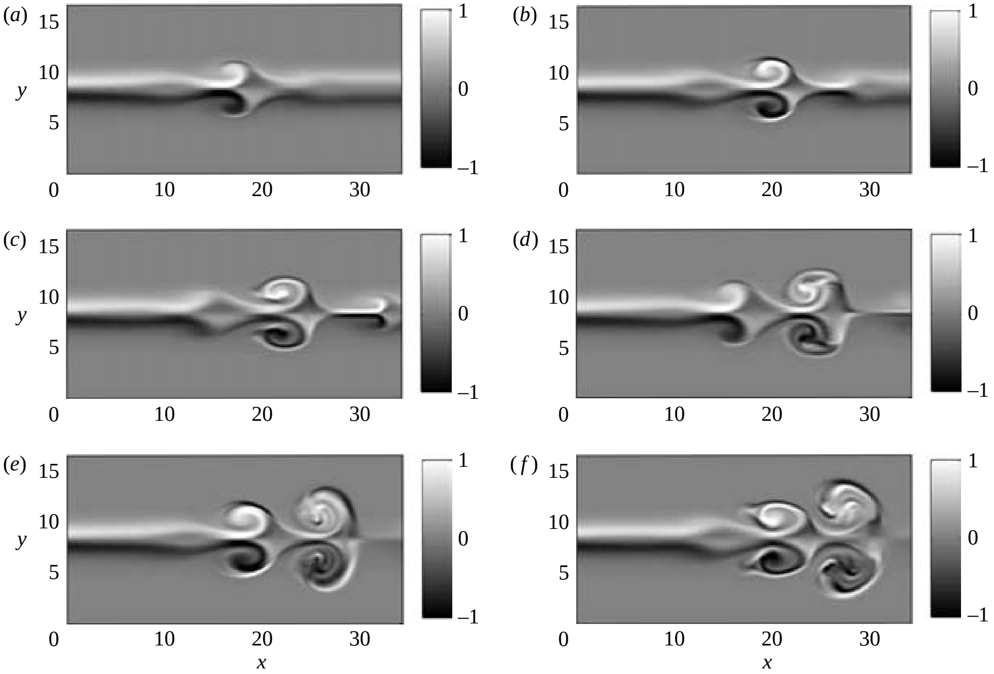

FIGURE 21. Sequence of a simulation after the convective/absolute transition (vorticity, $s = 0.1$, $N = 257$ and $n = 1$. Each view is separated by 300 time steps).

mainly with $N = 513$. For $s = 1$, before the linearly predicted transition which occurs at $s_{ca} = 0.935$, the jet behaves like an oscillator with the angular frequency of the transition and not in a convective fashion with the angular frequency of the maximum growth rate as one could expect. Different values of s, far from the transition, are then tried. It is found that the jet behaves like an oscillator for all the density ratios. For $s \geqslant 0.75$ (a nonlinear computed value) the oscillations are damped and ω depends on s. However, the oscillations are self-sustained for $s < 0.75$ with a well-defined angular frequency $\omega \simeq 0.66$ which is not the value predicted by linear instability theory. The main results of these computations are summed up in table 2 and in figures 22 to 26.

A plausible explanation of the behaviour of the top-hat-like jet as an oscillator for all the values of s used may be obtained by looking at the analytic dispersion relation of a top-hat jet ($n = \infty$). This relation reads (Huerre & Monkewitz 1990; Yu & Monkewitz 1993):

$$s\left(2-\frac{2\omega}{k}\right)^2 = \left(\frac{2\omega}{k}\right)^2 a(k), \tag{4.14}$$

where $a(k) = -\tanh(k)$ for the varicose mode and $a(k) = -1/\tanh(k)$ for the sinuous mode. Indeed, the calculations for $n = 4$, presented in figure 7, give a transition at $s_{ca} \simeq 0.93$ with an angular frequency equal to 0.77, a spatial growth rate equal to 1.19 and a wavenumber equal to 0.6. For a vortex sheet, the use of the dispersion relation (4.14) gives, at the same value of s, two saddle points near the real omega axis, $\mathrm{Re}(\omega)$, with $\mathrm{Im}(\omega_0) = \pm 0.05$, an angular frequency equal to 0.88, a spatial growth rate equal to 1.09 and a wavenumber equal to 0.42. This clearly shows that the vortex sheet approximation is, globally, a good one for the convective/absolute instability onset of the vortex layer with $n = 4$.

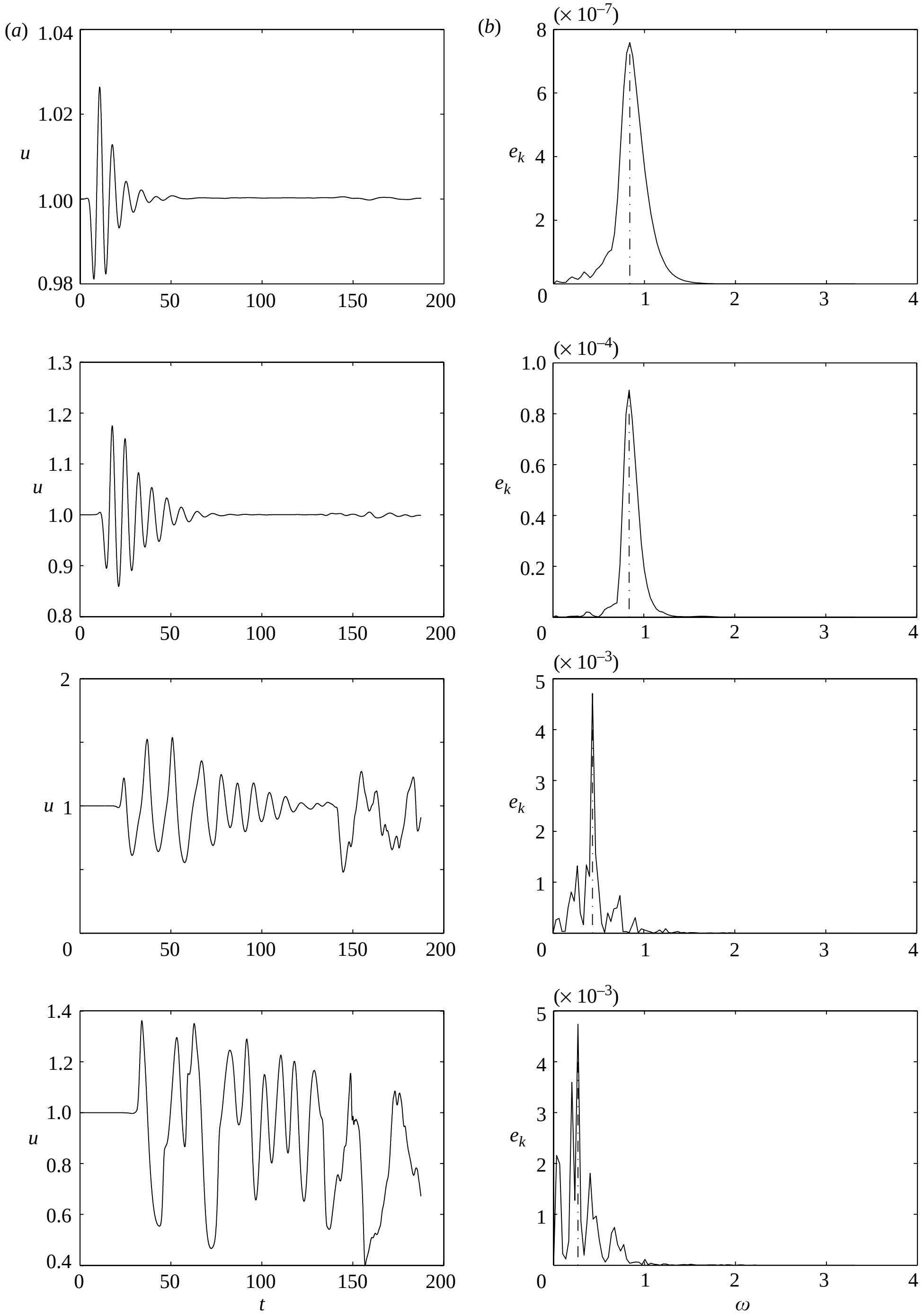

FIGURE 22. Global mode. From top to bottom, velocity u at 1/8, 1/4, 1/2, 3/4 of the computational domain for the top-hat-like jet. (a) $u(t)$; (b) the associated power spectrum $e_k(\omega)$ ($s = 1.2$, $n = 4$, $N = 257$, 6000 time steps are shown). This is a damped global behaviour at an angular frequency $\omega = 0.84$ with pairing in the second half part of the computational domain ($\omega = 0.44$ and $x > L_x/2$).

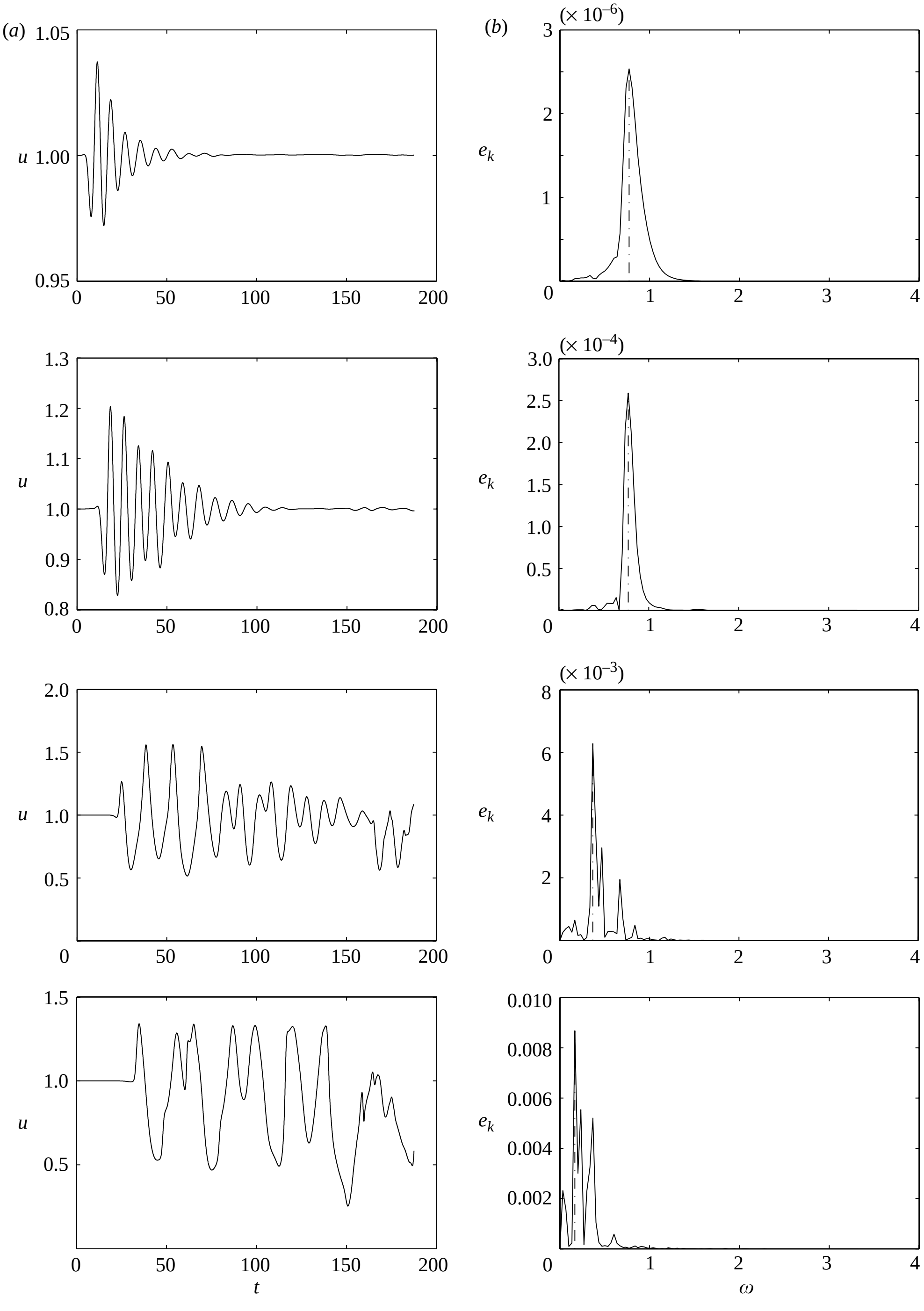

FIGURE 23. As figure 22, but $s = 1$. The angular frequency is $\omega = 0.77$ with pairing in the second half part of the computational domain ($\omega = 0.38$ and $x > L_x/2$).

Equation (4.14) presents the symmetry of a general Rayleigh equation: the solutions are complex conjugate. Furthermore it admits, for all s, two complex conjugate saddle points with $\mathrm{Re}(\omega_0)/\mathrm{Re}(k_0)$ not in the range of U_0 , i.e. $\mathrm{Re}(\omega_0)/\mathrm{Re}(k_0) > \max_y(U_0(y))$,

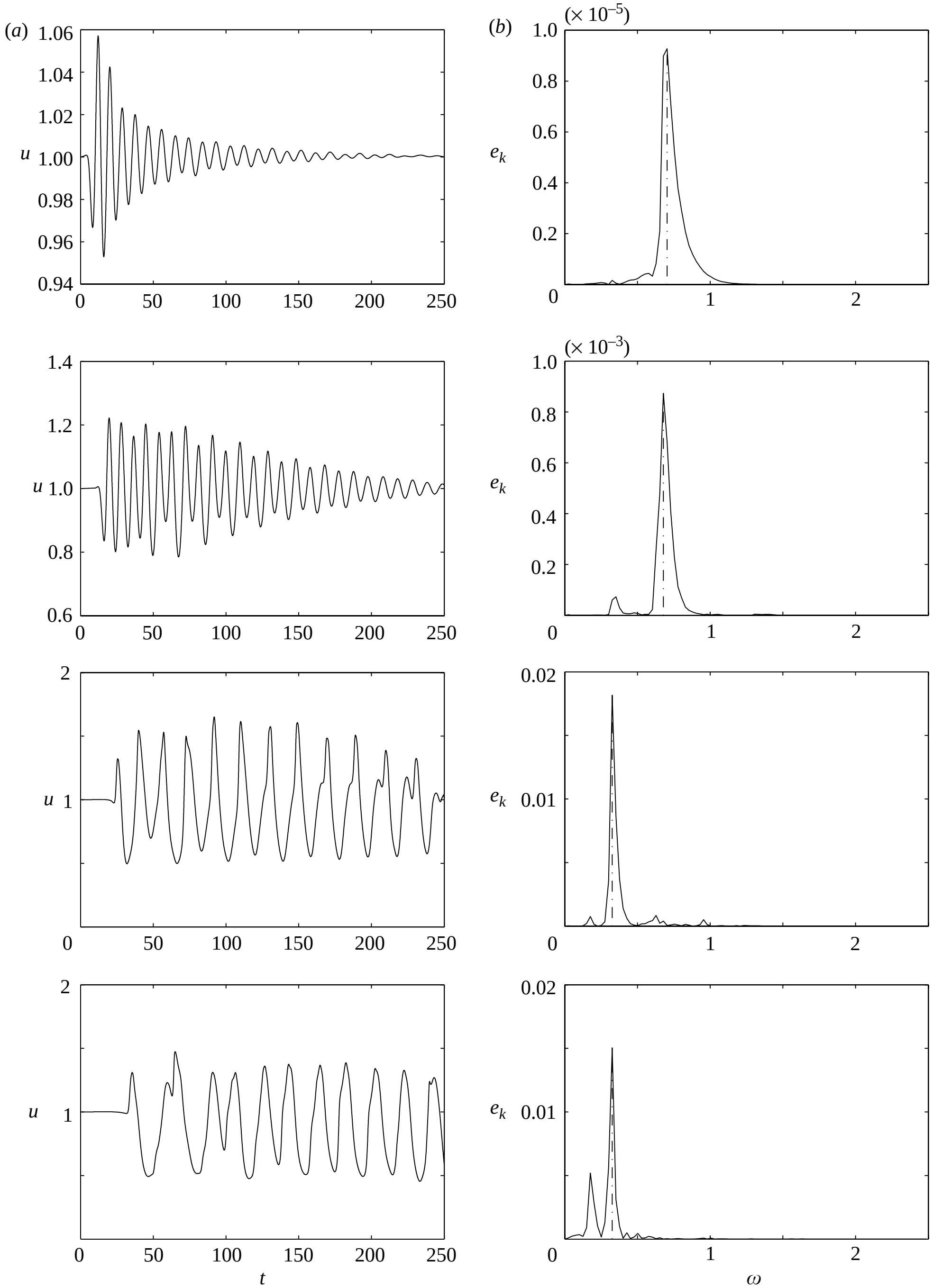

FIGURE 24. As figure 22, but $s = 0.8$ ($n = 4$, $N = 257$, 8000 time steps are shown). This is a damped global behaviour at an angular frequency $\omega = 0.68$ with pairing in the second half part of the computational domain ($\omega = 0.33$ and $x > L_x/2$).

as shown in figure 27 when $s = 1$ for example. This is also the case for $n = 4$ with $\mathrm{Re}(\omega_0)/\mathrm{Re}(k_0) = 1.28$. Therefore, the corresponding inviscid eigenfunctions are the asymptotic limits of the Orr–Sommerfeld ones as $Re \rightarrow \infty$ (Ledizès, Monkewitz &

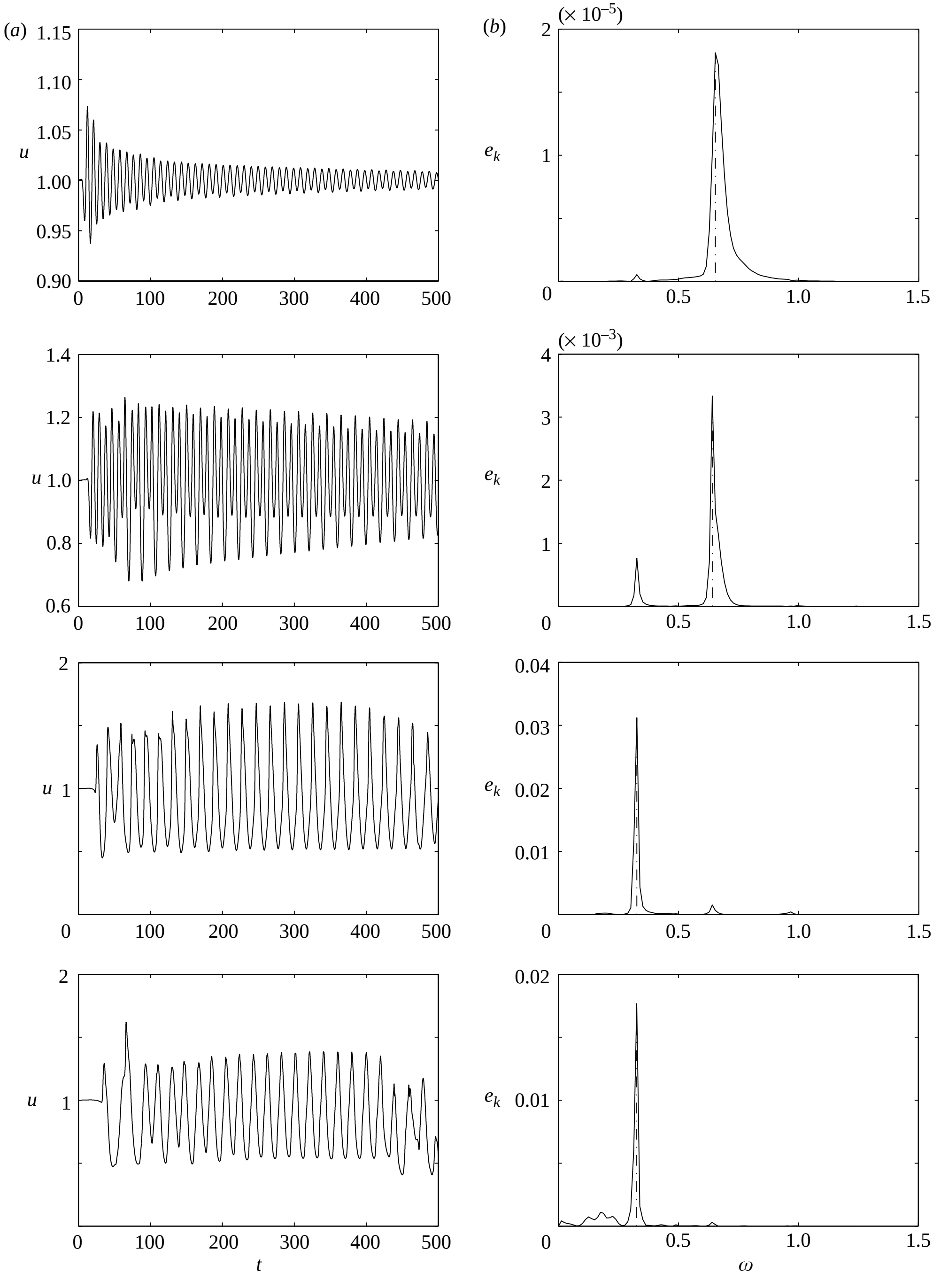

FIGURE 25. Global mode. From top to bottom, velocity u at 1/8, 1/4, 1/2, 3/4 of the computational domain for the top-hat-like jet. (*a*) $u(t)$; (*b*) the associated power spectrum $e_k(\omega)$ ($s = 0.7$, $n = 4$, $N = 257$, 16 000 time steps are shown). This is a self-sustained oscillator behaviour at an angular frequency $\omega = 0.67$ with pairing in the second half part of the computational domain ($\omega = 0.34$ and $x > L_x/2$).

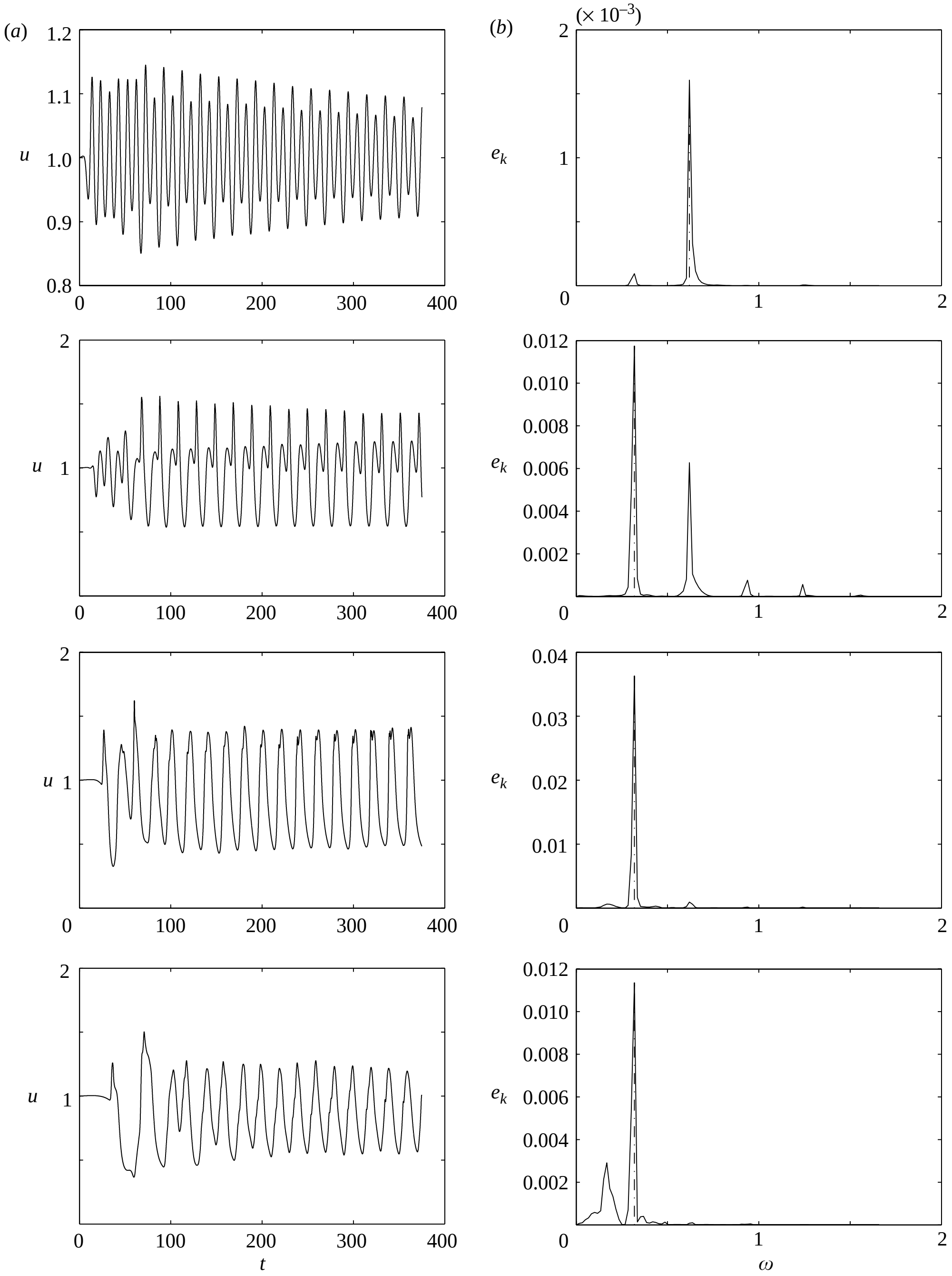

FIGURE 26. As figure 25, but $s = 0.5$ ($n = 4$, $N = 257$, 12 000 time steps are shown). This is a self-sustained oscillator behaviour at an angular frequency $\omega = 0.64$ with pairing in the second half part of the computational domain ($\omega = 0.34$ and $x > L_x/2$).

Huerre 1995). Consequently, the top-hat and, eventually, top-hat-like jets are absolutely unstable for all density ratios. So, the selected frequency is due to a nonlinear mechanism.

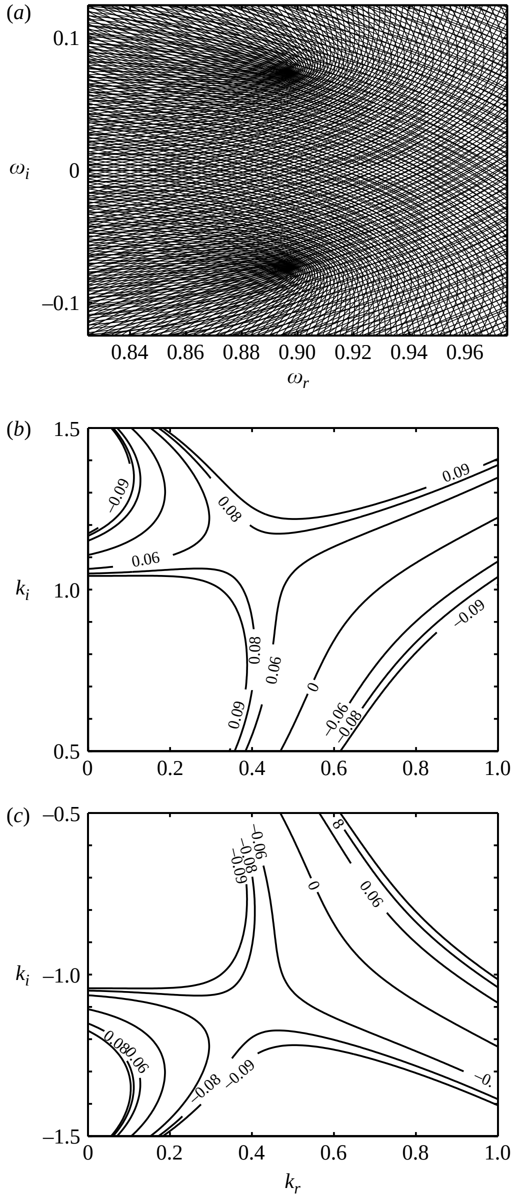

FIGURE 27. Complex conjugate saddle points of the Rayleigh equation when $n = \infty$ (top-hat profile) and $s = 1$: (*a*) in the complex ω-plane, (*b*) and (*c*) in the complex k-plane. Note that $\mathrm{Re}(\omega_0)/\mathrm{Re}(k_0)$ is greater than 1 and thus it is not in the range of U_0.

We may ask if the same arguments could be extrapolated to the Bickley jet? However, in this case, $\mathrm{Re}(\omega_0)/\mathrm{Re}(k_0)$ is in the range of U_0 and the extrapolation could be done only if there are no large viscous intervals, on the y-axis, where the Orr–Sommerfeld eigenfunction does not reduce to a solution of the Rayleigh equation when $Re \rightarrow \infty$ (Ledizès *et al.* 1995). However, if this is the case, s_{ca} should be understood as a convective/absolute transition from an always convectively unstable sinuous mode, for which no saddle point is found, to an always absolutely unstable varicose mode when lowering the density ratio. Indeed, according to the linear theory, when s decreases, the maximum growth rate of the varicose mode increases and overshoots the sinuous one. In fact, these extrapolations are wrong since the varicose initial perturbation, coming from initial conditions which are not exact solutions of the Navier–Stokes equations, are convected outside the domain. When lowering s, the varicose mode becomes marginal absolute and the nonlinear calculations show that the Bickley jet behaves as an oscillator, at the corresponding marginal angular frequency, for values of s far below s_{ca} according to Dee & Langer's selection criterion. Thus, the transition observed in the Bickley jet is really a convective/absolute transition of the varicose mode alone.

4.10.3. *Scenario of the density effect*

As we have seen in §4.10.2, a description based on the Dee & Langer (1983) criterion, although successful in the Bickley jet case in stating the density ratio effect, is not fully satisfactory in the top-hat-like jet case. We propose a scenario to complete this description in this paragraph.

For 'high' density ratios, jet dynamics is dictated by a linear mode selection in good qualitative agreement with the linear predictions presented in figure 3: the most unstable mode, the sinuous one, develops and forces the frequency of the jet. As density ratio decreases, the varicose mode becomes more and more unstable while the sinuous one becomes less and less so; the difference of growth rates between these two modes thus becomes smaller and smaller. When both modes have close growth rates, they can both coexist in the jet. For smaller density ratios, a global damped mode (the frequency is the same for the whole jet, but oscillations are slowly damped) exists for a small range of s values. When s is further decreased, there is a critical nonlinear value that we note s_{ca}^{NL} that could be different from the well-known s_{ca}^{lin} provided by a linear analysis below which the jet is absolutely unstable. In this case, the dynamics is essentially varicose and the frequency selection is made through a nonlinear process. The key point is that the absolute frequency depends on the density ratio s, but is not determined by the convective/absolute transition.

Results for $n = 4$ (top-hat-like) case are gathered in figure 28. Linear transition is symbolized with a diamond. It belongs to the area where the jet mode is global and damped (it is a convective mode, Huerre & Monkewitz 1985). The key transition is that of the varicose mode: it has a transition from a global and damped mode to a global and self-sustained, i.e. absolute, mode. The critical density ratio s_{ca}^{NL} is between 0.70 and 0.75. Let us emphasize that this value is in good agreement with that announced by Raynal *et al.* (1996) and the corresponding frequency is different from the 'box-frequency' one.

Finally, note that this scenario depends on the profile; for the Bickley jet ($n = 1$), the same scheme applies, but the transition density ratio is close, if not equal, to the linear prediction s_{ca}^{lin}.

4.10.4. *Note on the domain size and boundary effects*

As shown in table 2 (column 7), the nonlinear computations have been performed for different values of the domain size to gain confidence that the phenomena studied are not spurious. The same angular frequencies are obtained, when the domain size is varied (column 5), and they have nothing to do with 'box frequency' reported on the study of boundary effects by Buell & Huerre (1988). The box angular frequency is $\pi U_0(0)/L_x = 0.1$ (0.05 when doubling the domain length) and all the measured angular frequencies, of the physical phenomenon studied, are between 0.2 and 0.35 for

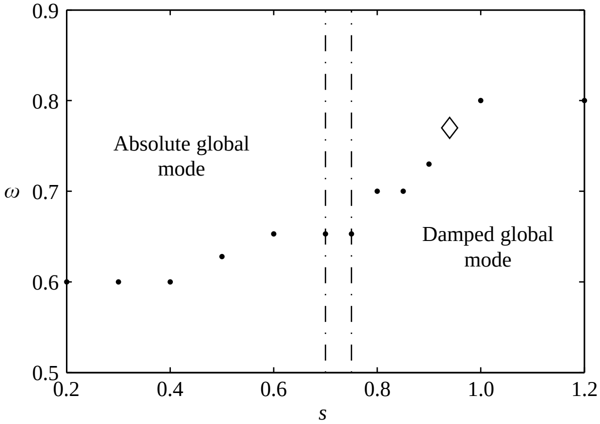

FIGURE 28. Angular frequency, ω, versus density ratio, s, of the varicose mode in the top-hat-like jet, ($n = 4$), case. There are two different domains: global damped (convective but with a well-defined frequency) and global self-sustained (absolute). The diamond represents the linear prediction of the transition that occurs at $s_{ca}^{lin} = 0.93$ whereas the nonlinear calculations give a nonlinear critical value $s_{ca}^{NL} \simeq 0.75$. Note that the angular frequencies obtained in the nonlinear calculations are different from the 'box angular frequencies': 0.1 and 0.05.

$n = 1$ and between 0.64 and 0.9 for $n = 4$. Furthermore, note that angular frequencies measured in the nonlinear calculations, of the present work, are in agreement with those predicted by the linear instability theory calculations presented in § 3. For example, for $n = 1$, $s = 0.13$, the angular frequency measured in the nonlinear calculation is 0.2 (Figure 20). The angular frequency predicted by linear calculations is 0.22 for $n = 1$, $s = 0.14$ from figure 5(*b*) for the pinching point (which corresponds to the most amplified unstable mode in this case). As another example, for $n = 4$, $s = 1$ the angular frequency measured in the nonlinear calculation is 0.77 (figure 23). The angular frequency predicted by linear calculations is also 0.77 from figure 7(*b*) for the pinching point. Clearly, this highlights the fact that measured frequencies, in the present nonlinear calculations, are not spurious because they are in agreement with linear predictions rather than with 'box frequency' or boundary effects.

4.10.5. *Associations of vortices: pairing*

Nonlinear terms may lead to coupling between vortices. Pairing may then be observed on temporal views or on the power spectrum of a temporal velocity signal (figure 29). On the power spectrum, it is found that the first subharmonic of the main frequency (the fundamental) is much more important than the main mode. This result was already established, experimentally, by Yu & Monkewitz (1993). It is also found, only for a varicose global mode with $n = 4$, that the fundamental is typically observed in the first quarter of the computational domain whereas the first subharmonic is observed in the remaining part as shown in figures 22 to 26.

4.11. *Reynolds-number influence*

All the simulation runs have been carried out for a Reynolds number arbitrarily set to a value of 1000. In this section, we will focus on the influence of this parameter. If the Reynolds-number value is lowered, then, the influence of dissipative effects is enhanced. The Reynolds-number influence depends on the value of the parameter n. We recall that, in the present study, the perturbations are not forced since the instabilities are only triggered by the initial dissimilarity between the initial velocity

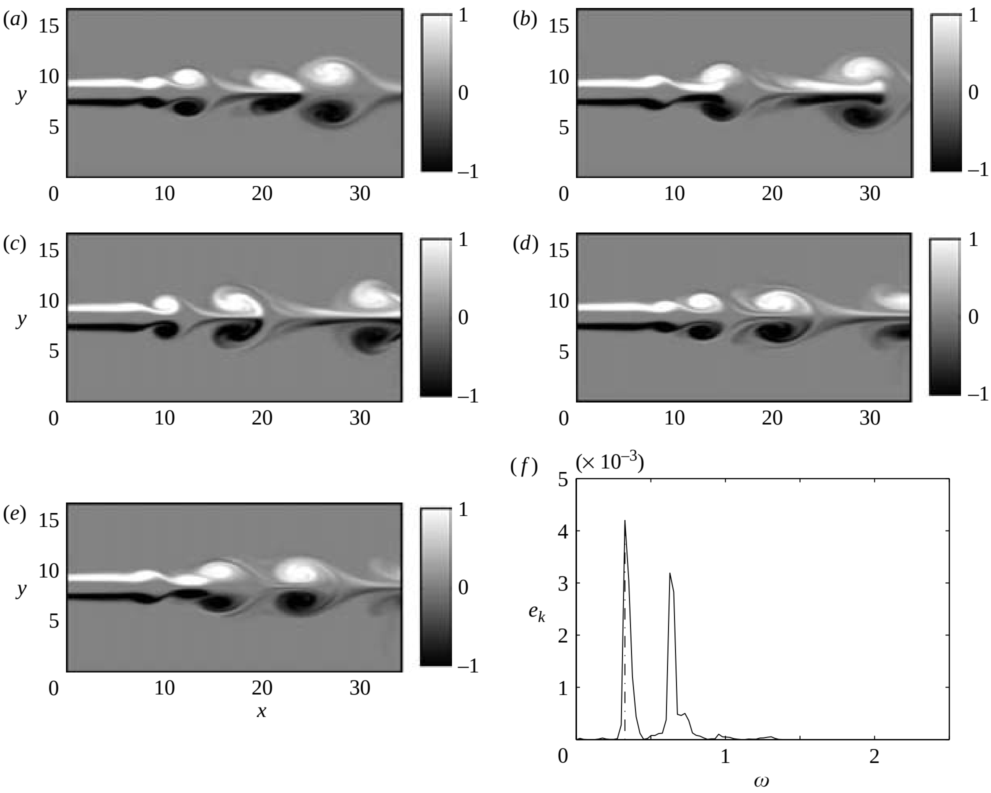

FIGURE 29. Pairing of vortices. (*a–e*) Successive views ($s = 0.8$, $N = 257$, each view is separated by 200 time steps) and (*f*) power spectrum of the temporal signal of the axial velocity. The first subharmonic ($\omega = 0.32$) of the main mode ($\omega = 0.64$) dominates the spectrum: this is an evidence of pairing.

profile and a steady laminar solution of the Navier–Stokes equations, and by the numerical truncation errors.

4.11.1. *The Bickley jet* $n = 1$

For the velocity profile with $n = 1$, the Reynolds number influence is not strong. For $Re > 400$, the differences we can observe with respect to the $Re = 1000$ case remain rather small, even though the viscous effects are felt as progressively becoming stronger; the appearance of the sinuous mode is delayed in time, but there is no change of the predictions nor of the nature of the observed dominant mode. In particular, note the following.

(i) For $s > 0.3$, there is no global mode. Only the sinuous mode can develop and it is of the convective type.

(ii) For $s = 0.2$, there is a damped global mode.

(iii) For $s = 0.1$, there is an absolute global mode with a frequency which almost does not change. Its angular frequency ω is reduced by about 10 %, from ($Re = 1000$) ω about 0.20 to ($Re = 400$) ω about 0.18.

For $Re = 200$, the global mode which is observed for $s = 0.10$ is not absolute anymore: it is damped. Therefore, for such dissipative effects, the critical density ratio s_{ca}^{NL} is significantly affected since, if it exists, its value is lower than 0.1. Indeed, as no simulation was performed for s smaller than 0.1, we could not display it.

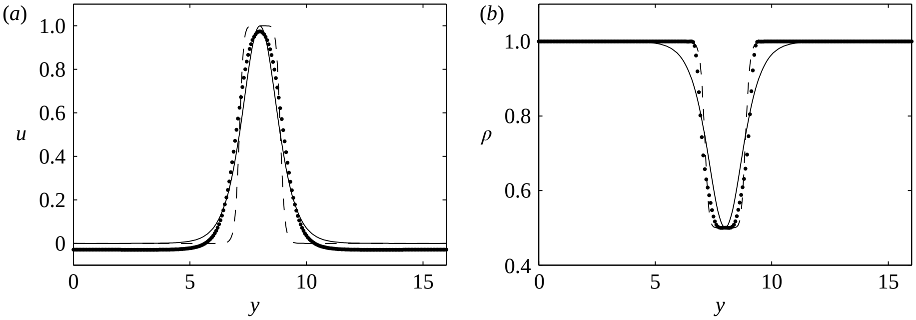

FIGURE 30. (*a*) Longitudinal velocity and (*b*) density profiles at $x = L_x/4$ for $Re = 200$ and $n = 4$ are presented with dots. The inlet velocity and density profiles (u_0, ρ_0) are presented, for comparison, with solid line in the $n = 1$ case and with dashed line in the $n = 4$ case. The velocity profile is modified by diffusion and it is close to that of the case $n = 1$.

When the Reynolds number becomes smaller than 150, the jet is almost stable: for the simulated durations (20 000 time steps for $N = 257$), no instability can develop before the 16 000th step (that is, three to four times later than for $Re = 1000$) and this development is very slow as compared to what is obtained for larger Reynolds numbers.

4.11.2. *The top-hat-like jet* $n = 4$

For the velocity profile with $n = 4$, trends are quite different. Indeed, for the Bickley jet, diffusion has little influence on the profile since it is associated with rather small gradients. On the contrary, for $n = 4$, it is observed that the main effect of viscous diffusion is to smooth out the velocity gradients and, to a smaller extent, the density gradients. For $Re = 800$, there is almost no difference with respect to $Re = 1000$. For $Re = 600$, the global mode for $s = 0.7$ is not self-sustained anymore, but damped. The critical value of the density ratio is then estimated as being $s_{ca}^{NL}(Re = 600) = 0.5$. The angular frequency of the self-sustained global mode for $s = 0.3$ is switched from $\omega(Re = 1000) = 0.60$ to $\omega(Re = 600) = 0.51$.

For Reynolds numbers smaller than 400, the profile is significantly changed so that it is not possible anymore to say that the profile corresponds to $n = 4$. Indeed, as figure 30 shows, the velocity profile which is obtained at $x = L_x/4$ after advection of the initial perturbation (during the time for which the jet is laminar before the sinuous instability can develop) is very close to those obtained for the Bickley jet. It is then not surprising to find the sinuous mode, even for $s = 0.5$. The density profile is also modified, but by a smaller amount: it still displays a plateau in the central region, which the velocity profile does not display, and the differences with respect to the mean profile which is obtained for $Re = 600$ are not significant.

Therefore, for $n = 4$, when the Reynolds number is decreased, the basic flow is modified and it tends to become like that for $n = 1$, but it never exactly reaches it since the condition with $n = 4$ is still imposed right in the entry section.

5. Conclusion

Free evolving, variable-density and incompressible plane jets have been studied in the linear and nonlinear regimes. The linear study was performed using diagonalization and shooting, two complementary methods, to solve the variable-density Rayleigh equation both in temporal and spatial stability frameworks. It is

n	Mode	s_{ca}	$\omega_r^0(k_0; s_{ca})$	$\omega_r(\max(-k_i); s_{ca})$	Re
1	Sinuous	–	–	–	∞
1	Varicose	0.145	0.21	0.21	∞
4	Sinuous	–	–	–	∞
4	Varicose	0.935	0.77	1.07	∞

TABLE 1. Summary of linear predictions.

n	s	Observed mode	$\dfrac{s - s_{ca}}{s_{ca}}$	ω	$\dfrac{\omega - \omega_r^0(k_0; s_{ca})}{\omega_r^0(k_0; s_{ca})}$	L_x	$\dfrac{L_x}{L_y}$	N	$\dfrac{\delta_\omega}{L_y}N$	T	Re
1	1	Sinuous	–	0.35	–	32; 64	2	129; 257	10; 20	480	700; 1000
1	0.3	Sinuous	–	0.25	–	32; 64	2	129; 257	10; 20	650	700; 1000
1	0.2	Varicose	0.38	0.2	−0.05	32; 64	2	129; 257	10; 20	650	700; 1000
1	0.13	Varicose	−0.1	0.2	−0.05	32; 64	2	129; 257	10; 20	650	700; 1000
1	0.1	Varicose	−0.31	0.21	0	32; 64	2	129; 257	10; 20	650	700; 1000
4	1.5	Varicose	0.6	0.9	0.17	32; 64	2	257; 513	5; 10	250	700; 1000
4	1.2	Varicose	0.27	0.85	0.10	32; 64	2	257	5	250	700; 1000
4	1	Varicose	0.07	0.77	0	32; 64	2	257; 513	5; 10	250	700; 1000
4	0.8	Varicose	−0.14	0.68	−0.12	32; 64	2	257; 513	5; 10	250	700; 1000
4	0.7	Varicose	−0.25	0.67	−0.13	32; 64	2	257; 513	5; 10	250	700; 1000
4	0.6	Varicose	−0.36	0.64	−0.17	32; 64	2	257; 513	5; 10	250	700; 1000

TABLE 2. Summary of nonlinear results.

found that the jet is subject to varicose (asymmetrical deformation) and sinuous (symmetrical deformation) unstable modes. When the density is constant, the sinuous mode dominates. Lowering the density enhances the varicose mode which becomes dominant before undergoing a convective/absolute transition. Only the varicose mode is found to present such a transition. The main results of the linear study are summarized in table 1. The pertinence of these linear results to a more realistic nonlinear evolution was then tackled by direct numerical simulation of the incompressible variable-density Navier–Stokes equations. A computational procedure has been developed based on a multigrid method to solve the pressure equation which is more complicated than the classical Laplace equation that we obtain in the constant density case. Many boundary conditions are tested and the best ones are reported. The procedure developed has been checked by reproducing the linear results, obtained in the first part of the study, when the nonlinear terms of the Navier–Stokes equations are linearized about a main profile. Once the procedure is tested, nonlinear computations are conducted and the main results are summarized in table 2. The nonlinear study has shown that for the Bickley jet, $n = 1$, the nonlinear evolution is predicted well by a local linear marginal absolute instability criterion: the jet undergoes self-sustained oscillations (global mode) at a well-defined frequency with a corresponding Strouhal number $S_t \simeq 0.06$, based on the jet diameter, for a density ratio $s < s_{ca} = 0.145$. These values coincide with those computed linearly by a local convective/absolute transition. Contrarily, for the top-hat-like jet, $n = 4$, the linear study fails: it predicts global behaviour for $s < s_{ca} = 0.935$ and a corresponding Strouhal number $S_t \simeq 0.25$. However, global modes are nonlinearly observed for all the values of s used. For $s \geqslant 0.75$ (a nonlinear computed value) the oscillations are damped and S_t depends on s. The oscillations are self-sustained for $s < 0.75$ with a well-defined $S_t \simeq 0.21$. This may explain the discrepancy between the experimental studies of Yu & Monkewitz and those of Raynal *et al.*: for a top-hat (or a top-hat-like) jet, global behaviour is possible for all the values of s, but self-sustained oscillations are favoured for $s < 0.75$ and therefore are much more likely to occur in that range in agreement with the $s < 0.7$ found in the experimental work of Raynal *et al.* A tentative explanation of the global behaviour observed in the top-hat-like jet for all values of s is also given. It is based on solutions of the Squire equation that are also solutions of the Rayleigh equation, in the limit $R_e \to \infty$, when the phase velocity is greater than one.

Fruitful discussions with S. Ledizès, P. A. Monkewitz and E. Villermaux are acknowledged.

Appendix A. Spatial discretization

For the spatial discretization, finite-difference schemes are used:

(i) centred in the inner of the computation domain,

(ii) not centred but second-order accurate on the borders.

Special attention is paid to border formulae since the lowest order in the domain limits the global order for all the simulations. Since computation time and complexity (boundary conditions especially) increase faster than benefits, no high-order methods are used. With such a discretization scheme, the multigrid method to solve (4.1) is more straightforward. For an inner grid mesh point:

$$\left.\frac{\partial a}{\partial x}\right|_{(i,j)} = \frac{1}{2\,h_x}\left(a_{(i+1,j)} - a_{(i-1,j)}\right),$$

$$\left.\frac{\partial a}{\partial y}\right|_{(i,j)} = \frac{1}{2\,h_y}\left(a_{(i,j+1)} - a_{(i,j-1)}\right),$$

and for the second-order derivatives,

$$\left.\frac{\partial^2 a}{\partial x^2}\right|_{(i,j)} = \frac{1}{h_x^2}\left(a_{(i+1,j)} - 2\,a_{(i,j)} + a_{(i-1,j)}\right),$$

$$\left.\frac{\partial^2 a}{\partial y^2}\right|_{(i,j)} = \frac{1}{h_y^2}\left(a_{(i,j+1)} - 2\,a_{(i,j)} + a_{(i,j-1)}\right).$$

For the points on the border of the grid, the formulae are

$$\left.\frac{\partial a}{\partial x}\right|_{(1,j)} = \frac{1}{2\,h_x}\left(-3\,a_{(1,j)} + 4\,a_{(2,j)} - a_{(3,j)}\right),$$

$$\left.\frac{\partial a}{\partial x}\right|_{(N,j)} = \frac{1}{2\,h_x}\left(3\,a_{(N,j)} - 4\,a_{(N-1,j)} + a_{(N-2,j)}\right),$$

and

$$\left.\frac{\partial^2 a}{\partial x^2}\right|_{(1,j)} = \frac{1}{h_x^2}\left(2\,a_{(1,j)} - 5\,a_{(2,j)} + 4\,a_{(3,j)} - a_{(4,j)}\right),$$

$$\left.\frac{\partial^2 a}{\partial x^2}\right|_{(N,j)} = \frac{1}{h_x^2}\left(2\,a_{(N,j)} - 5\,a_{(N-1,j)} + 4\,a_{(N-2,j)} - a_{(N-3,j)}\right)$$

which are second-order accurate. The similar formulae for y derivatives are straightforward.

Appendix B. Solution of the pressure equation

To solve the linear elliptic equation of pressure with appropriate boundary conditions:

$$\nabla\cdot\left(\frac{1}{\rho}\nabla p\right)=\nabla\cdot\left(\frac{\boldsymbol{v}^{\star}}{\Delta t}\right) \quad \text{in} \quad \Omega, \tag{B 1}$$

$$B(p)=0 \quad \text{in} \quad \partial\Omega, \tag{B 2}$$

which is more complicated than the Poisson equation, that would be obtained for a homogeneous fluid, a multigrid method is used. This method presents the advantage of solving the equations (B 1) and (B 2), discretized on N^2 two-dimensional grid points, in $O(N^2\log(N))$ operations, which is comparable to FFT based methods. As ‘Unfortunately there is not a single multigrid algorithm that solves all elliptic problems. Rather there is a multigrid technique that provides the framework of solving these problems’ (Press 1992), this section is devoted to a description of the method inspired by Briggs & Henson (1987) and used in the present study.

For its ease of implementation, a central finite-difference technique is used to discretize equations (4.4) and (4.5) on a uniform grid G^h of mesh size h. Let $\nabla^h=(\delta^h/r,\delta^h)$ denote the approximate gradient on G^h, δ^h the finite-difference approximation of the spatial partial first derivative given in § 4.4 and r the aspect ratio of the rectangular computational domain. (The use of the aspect ratio transfers the geometrical anisotropy of the grid to the pressure equation and offers the comfort of using a square mesh and thus treats x and y directions in the same way.) Then, the approximate pressure equation, on G^h, can be written as a system of linear equations:

$$A^h p^h = f^h, \tag{B 3}$$

Where:

$$A^h=\nabla^h\cdot\left(\frac{1}{\rho^h}\nabla^h\right) \quad \text{on} \quad G^h, \quad A^h=B^h \quad \text{on} \quad \partial G^h,$$

$$f^h=\nabla^h\cdot\left(\frac{\boldsymbol{v}^{\star h}}{\Delta t}\right) \text{on} \quad G^h, \quad f^h=0 \quad \text{on} \quad \partial G^h.$$

The detailed expression of the linear operator A^h is very lengthy and complicated and thus not given in the present paper.

Let v^h denote an approximation to the exact solution of the difference equation (B 3). Then the residue, r^h, and the error (the correction), e^h, satisfy the following equations:

$$r^h=f^h-A^h v^h, \quad A^h e^h=A^h(p^h-v^h)=r^h.$$

The multigrid technique uses the smoothing property of some relaxation schemes, such as the Gauss–Seidel one used in the present calculations, successively on coarser and coarser grids $G^{2h}, G^{4h}, G^{8h}, \ldots, G^{(N_g-1)2h}$ (the descending phase) to obtain a good approximation of the error (the correction) on successively finer and finer grids, $\ldots$, $G^{8h}, G^{4h}, G^{2h}, G^h$ (the ascending phase). In this notation, N_g is the grid number and is related to the grid resolution N by $N=2^{N_g}+1$. The travel between the different grids is ensured by the restriction operator I_h^{2h} in the descending phase and by the prolongation operator I_{2h}^{h} in the ascending phase. A pair of descending–ascending phases is called a V-cycle. A V-cycle can be treated with a recursive procedure:

```
$v^h \leftarrow V^h(v^h, f^h)$
        1. Relax $\alpha_1(h)$ times on $A^h v^h = f^h$.
        2. If $G^h$ is the coarsest grid relax $\alpha_2$ times on $A^h v^h = f^h$.
        Else: $f^{2h} \leftarrow I_h^{2h}(f^h - A^h v^h)$
              $v^{2h} \leftarrow 0$
              $v^{2h} \leftarrow V^{2h}(v^{2h}, f^{2h})$
              Correct $v^h \leftarrow v^h + I_{2h}^{h} v^{2h}$
              Relax $\alpha_1(h)$ times on $A^h v^h = f^h$.
```

In the present calculations the following restriction and prolongation operators are used:

$$I_h^{2h} = \begin{bmatrix} \frac{1}{16} & \frac{1}{8} & \frac{1}{16} \\ \frac{1}{8} & \frac{1}{4} & \frac{1}{8} \\ \frac{1}{16} & \frac{1}{8} & \frac{1}{16} \end{bmatrix}, \quad I_{2h}^{h} = \begin{bmatrix} \frac{1}{4} & \frac{1}{2} & \frac{1}{4} \\ \frac{1}{2} & 1 & \frac{1}{2} \\ \frac{1}{4} & \frac{1}{2} & \frac{1}{4} \end{bmatrix},$$

where the coefficients must be interpreted as the fractions of the neighbouring values the central point receives, in the restriction case, and the fractions of its own value the central point gives to its neighbours in the prolongation case. These operators verify the Galerkin condition (Briggs & Henson 1987; Press 1992).

Many fashions of combining V-cycles lead to different multigrid methods. The simplest one, that consists in applying successively many V-cycles, is used. In practice, it is found, for example, that only five V-cycles are sufficient to reduce the residue norm, inside G, by a factor of 10^3 with $N = 129$, $\alpha_1(h) = \mathrm{int}(80\,h^{0.6} + 2)$[†], $r = 2$ and $\alpha_2 = 100$. As the temporal simulations will be started with a quasi-incompressible velocity field giving initial residue norm $O(10^{-3})$, this residue will be $O(10^{-6})$ after five or six V-cycles. Then, the choice of small Δt will maintain the residue norm to that value with approximately the same number of V-cycles overall the simulation.

Finally, Dirichlet ($B = \text{Identity}$) and Neumann ($B = \partial/\partial n$, n is the normal direction to $\partial\Omega$) boundary conditions are used. It is found that the Neumann boundary condition is more appropriate for the jet flow (The Dirichlet boundary condition prevents the jet from leaving Ω). However, with Neumann boundary condition, the problem is ill posed in the sense that the pressure is determined up to an undetermined constant. This does not matter since only the gradient of the pressure is used in the momentum equations. Furthermore, to eliminate the high-wavenumber oscillations of the pressure solution, owing to the use of central finite differences on a non-staggered grid, a compact spatial filter, that confines its effect to high wavenumbers, is used as explained in Appendix C.

Appendix C. Spatial filtering

In a one-dimensional grid of mesh size h, the minimum wavelength is $2h$ corresponding to a maximum wavenumber $k_{max} = 2\pi/(2h) = \pi/h$. The spatial filtering in a direct numerical simulation with central finite differences can be justified by

---

[†] Note that for the same time of calculation, the variable number of relaxation sweeps $\alpha_1(h) = \mathrm{int}(80\,h^{0.6} + 2)$ is twice more efficient than $\alpha_1 = 7 = \text{constant}$ in reducing the residue by the same factor.

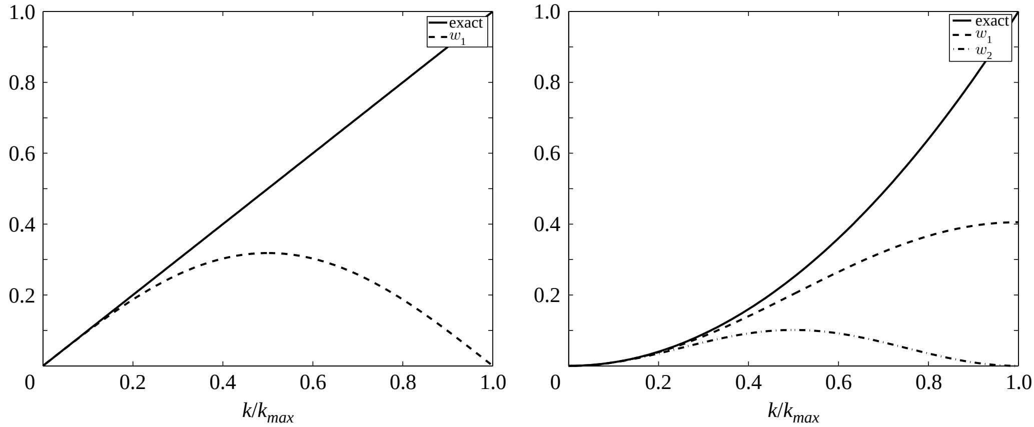

FIGURE 31. Plot of modified wavenumbers versus normalized wavenumbers for (*a*) the first derivative approximation and (*b*) for the second derivative approximation. –, exact; - - -, w_1; ·—·, w_2.

looking at the truncation errors of the differences in the wavenumber space (Fourier space). Using h as a length scale, the exact first derivative of a Fourier mode, $\exp(\mathrm{i}kx)$, is $\mathrm{i}k\exp(\mathrm{i}kx)$ while using the first derivative central difference formula we obtain:

$$\frac{\exp(\mathrm{i}k(x+1)) - \exp(\mathrm{i}k(x-1))}{2} = \mathrm{i}\sin(k)\exp(\mathrm{i}kx),$$

leading to a modified wavenumber (Lele 1992) $w_1(k) = \sin(k)$, $k \in [0, \pi]$. In the same way, the second derivative central difference formula gives $w_2(k) = 2(1 - \cos(k))$ and applying successively twice the first derivative formula gives $w_2'(k) = (1 - \cos(2k))/2$. These modified wavenumbers are plotted in figure 31. It is evident from these figures that to obtain better resolved wavenumbers, the grid must be refined ($k_{max}h = \pi = \text{constant}$). Furthermore, for wavenumbers $k \geqslant k_{max}/2$ a poor approximation to the derivatives is obtained independently from the resolution. Thus, this range of wavenumbers can be treated by a filter that confines its effects in that range. In addition, the filter can be designed to eliminate exactly the highest wavenumber k_{max} which is a pathological solution of the discretized pressure equation (4.4). Compact filters can do this work very well. Let f_j denote a function value at nodes $x_j = h(j-1)$, $1 \leqslant j \leqslant N$ and $\check{f}_j$ the filtered values. A fourth-order compact filter (Lele 1992; Slinn & Riley 1998) that requires solution of a tridiagonal matrix is used. It can be formulated in the following way:

$$\alpha_1 \check{f}_{j-1} + \check{f}_j + \alpha_1 \check{f}_{j+1} = a_1 f_j + \tfrac{1}{2} b_1 (f_{j+1} + f_{j-1}) + \tfrac{1}{2} c_1 (f_{j+2} + f_{j-2}).$$

Using h as a length scale, the corresponding transfer function, $T(k)$, defined by $\widehat{\check{f}_j} = T(k)\widehat{f_j}$, with Fourier mode solutions:

$$f_j = \widehat{f_j}\exp(\mathrm{i}kj), \quad \check{f}_j = \widehat{\check{f}_j}\exp(\mathrm{i}kj), \quad k \in [0, \pi],$$

reads:

$$T(k) = \frac{a_1 + b_1\cos(k) + c_1\cos(2k)}{1 + 2\alpha_1\cos(k)}.$$

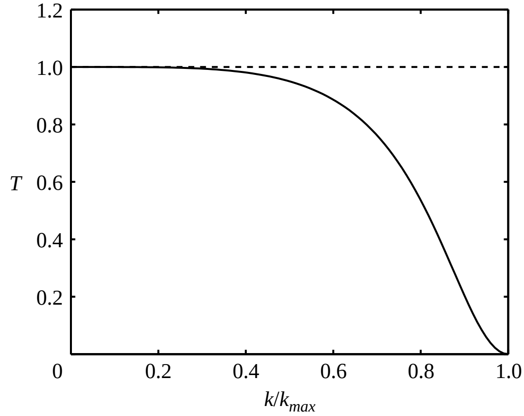

FIGURE 32. –, Plot of the transfer function of the fourth-order compact filter with $\alpha_1 = 0.4$. - - -, no filter. Note that most of its effects are confined to $k/k_{max} \geqslant 0.5$.

A family of fourth-order compact filters can be generated when the constraints

$$T(\pi) = 0, \quad \frac{\mathrm{d}T}{\mathrm{d}k}(\pi) = 0.$$

are added. (Note that the first constraint is exactly what is needed to eliminate the highest wavenumber pathological solution of the pressure equation if the filter is applied to the pressure.) The coefficients of the filter are then:

$$a_1 = \tfrac{1}{8}(5 + 6\alpha_1), \quad b_1 = \tfrac{1}{2}(1 + 2\alpha_1), \quad c_1 = \tfrac{-1}{8}(1 - 2\alpha_1).$$

A filter with $\alpha_1 = 0.4$ is used and the corresponding transfer function is plotted on figure 32. For the boundary nodes, explicit fourth-order formulation that exactly filters $k = \pi$ wave is used:

$$\check{f}_1 = \tfrac{15}{16} f_1 + \tfrac{1}{16}(4f_2 - 6f_3 + 4f_4 - f_5),$$
$$\check{f}_2 = \tfrac{3}{4} f_2 + \tfrac{1}{16}(f_1 + 6f_3 - 4f_4 + f_5).$$

Finally, to obtain a two-dimensional filter, two sweeps of the one-dimensional filter are orthogonally applied and a check that the relative energy of the filtered function is diminished by less than 10^{-6}, compared to that of the initial function, is performed.

REFERENCES

BERS, A. 1983 *Space–Time Evolution of Plasma Instabilities – Absolute and Convective*. Handbook of Plasma Physics (ed. A. A. Galeev & R. N. Sudan), vol. 1: Basic Plasma Physics I, chap. 3.2, pp. 451–517. North-Holland.

BHAGANAGAR, K., REMPFER, D. & LUMLEY, J. 2000 3-D simulation of transition to turbulence in a flat-plate boundary layer. In *8th Annual Conf. of the CFD Society of Canada*.

BOERSMA, B. J., BRETHOUWER, G. & NIEUWSTADT, F. T. 1998 A numerical investigation on the effect of the inflow conditions on the self-similar region of a round jet. *Phys. Fluids* **10**, 899–909.

BRIGGS, W. L. & HENSON, V. E. 1987 A multigrid tutorial. In *Third Copper Mountain Conf. on Multigrid Methods*.

BUELL, J. C. & HUERRE, P. 1988 Inflow/outflow boundary conditions and global dynamics of spatial mixing layers. *Center for Turbulence Res.* pp. 19–27.

DEE, G. & LANGER, J. S. 1983 Propagating pattern selection. *Phys. Rev. Lett* **50**, 383.

DELBENDE, I. & CHOMAZ, J.-M. 1998 Nonlinear convective/absolute instabilities in parallel two-dimensional wakes. *Physics of Fluids* **10**, 2724–2736.

Delbende, I., Chomaz, J.-M. & Huerre, P. 1998 Absolute/convective instabilities in the Batchelor vortex: a numerical study of the linear impulse response. *J. Fluid Mech.* **355**, 229–254.

Drazin, P. & Reid, W. 1982 *Hydrodynamic Stability*. Cambridge University Press.

Givoli, D. 1991 Non-reflecting boundary conditions. *J. Comput. Phys.* **94**, 1–29.

Gresho, P. M. 1991 Incompressible fluid dynamics: some fundamental formulations issues. *Annu. Rev. Fluid Mech.* **23**, 413–453.

Huerre, P. & Monkewitz, P. A. 1985 Absolute and convective instabilities in free shear layers. *J. Fluid Mech.* **159**, 151–168.

Huerre, P. & Monkewitz, P. A. 1990 Local and global instabilities in spatially developing flows. *Annu. Rev. Fluid Mech.* **22**, 473–537.

Kyle, D. & Sreenivasan, K. R. 1993 The instability and breakdown of a round variable-density jet. *J. Fluid Mech.* **249**, 619–664.

Landau, L. D. & Lifshitz, I. M. 1959 *Fluid Mechanics*. Pergamon.

Ledizès, S., Monkewitz, P. A. & Huerre, P. 1995 Viscous structure of plane waves in spatially developing shear flows. *Phys. Fluids* **6**, 1337–1347.

Lele, S. K. 1992 Compact finite difference schemes with spectral-like resolution. *J. Comput. Phys.* **103**, 16–42.

Mattingly, G. E. & Criminale Jr, W. 1971 Disturbance characteristics in a plane jet. *Phys. Fluids* **14**, 2258–2264.

Monkewitz, P. A., Bechert, D. W., Barsikow, B. & Lehmann, B. 1990 Self-excited oscillations and mixing in a heated round jet. *J. Fluid Mech.* **213**, 611–639.

Pier, B. & Huerre, P. 2001 Nonlinear self-sustained structures and fronts in spatially developing wake flows. *J. Fluid Mech.* **435**, 145–174.

Press, W. H. (ed.) 1992 *Numerical Recipes*. Cambridge University Press.

Raynal, L., Harion, J.-L., Favre-Marinet, M. & Binder, G. 1996 The oscillatory instability of plane variable-density jets. *Phys. Fluids* **8**, 993–1006.

Slinn, D. N. & Riley, J. 1998 A model for the simulation of turbulent boundary layers in an incompressible stratified flow. *J. Computat. Phys.* **144**, 550–602.

Sreenivasan, K. R., Raghu, S. & Kyle, D. 1989 Absolute instability in variable density round jets. *Exps. Fluids* **7**, 309–317.

Stanley, S. A., Sarkar, S. & Mellado, J. 2002 A study of the flow-field evolution and mixing in a planar turbulent jet using direct numerical simulation. *J. Fluid Mech.* **450**, 377–407.

Twiss, R. Q. 1951 On oscillations in electron streams. *Proc. Phys. Soc.* B **64**, 654.

Yu, M.-H. & Monkewitz, P. A. 1990 The effect of nonuniform density on the absolute instability of two-dimensional inertial jets and wakes. *Phys. Fluids* A **2**, 1175–1181.

Yu, M.-H. & Monkewitz, P. A. 1993 Oscillations in the near field of a heated two-dimensional jet. *J. Fluid Mech.* **255**, 323–347.